Rimar
Congress
baghdad

مؤتمر ريمار الدولي السابع للعلوم الصرفة والتطبيقية

VII. International Rimar Congress of Pure, Applied Sciences

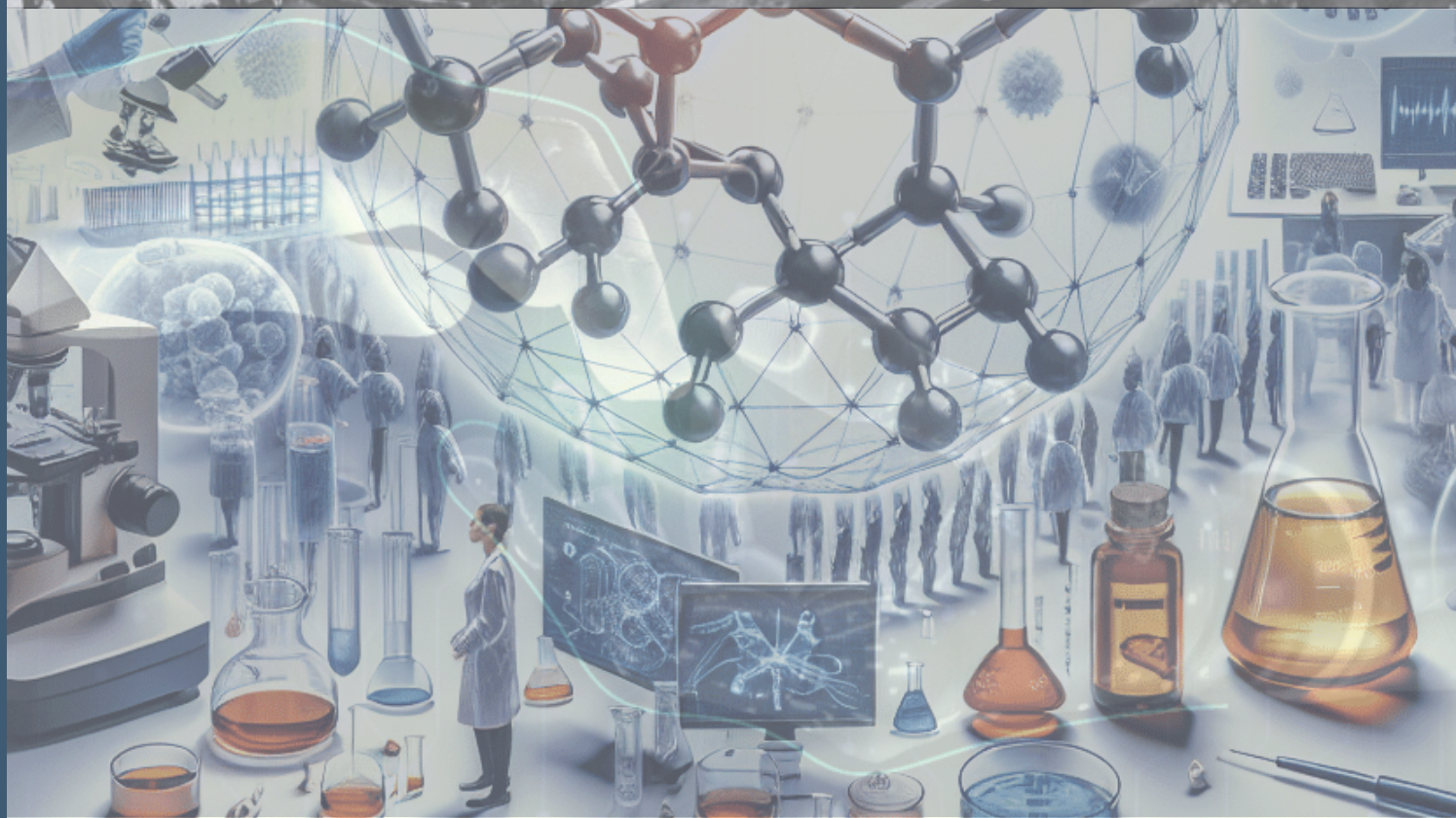

2025

FULL TEXT BOOK

RIMAR ACADEMY

مؤتمر ريمار الدولي السابع للعلوم الصرفة والتطبيقية

FULL TEXT BOOK

كتاب الوقائع

2025

ISBN 978-625924399-3

Publishing House:	دار النشر:	Rimar Academy
Editor:	المحرر:	Prof. Dr. Ghuson H. MOHAMMED
Publication Coordinator:	تنسيق النشر:	AMIR MUAENI
ISBN:	نظام الترميز الدولى لترقيم الكتاب:	978-625-92439-9-3
DOI :	رقم معرف الكائن الرقمي:	http://dx.doi.org/10.47832/RimarCongress07
Printing:	تاريخ الطباعة:	2026 / 02 / 29
Date of The Congress:	تاريخ المؤتمر:	2025 / 12 / 20 - 19 - 18
Pages:	عدد الصفحات:	31
URL :	رابط النشر:	www.rimaracademy.com
Certificate Printing Press Number	رقم شهادة المطبعة:	47843

PREFACE

VII. International Rimar Congress of Pure, Applied Sciences was organized by Mardin University in collaboration with Rimar Academy. The primary objective of this event was to compile and disseminate valuable scientific knowledge andmake ameaningful contribution to the future.

A substantial number of researchers from both local and international backgrounds demonstrated their interest in this conference. The scientific committee meticulously reviewed the submissions and ultimately accepted a select group of applicants—**15** in total—of whom **10** were approved by the scientific committee.

The core of this conference was the presentation of **9** full research papers, while the remaining articles and research findings are set to be featured in for the coming issues of the MINAR Journal.

I would like to extend my sincere appreciation to all the contributors and scholars who played an essential role in making this conference a resounding success.
Your dedication and valuable contributions are deeply respected and acknowledged.

Editor-in-Chief
Prof. Dr. Ghuson H. MOHAMMED

رئيس المؤتمر
Chair of Congress

Chair of Congress

رئيس المؤتمر

الأستاذ الدكتور غصون حميد محمد

Prof. Dr. Ghuson H. MOHAMMED

جامعة بغداد

Baghdad University

Iraq - العراق

Chairman of Organizing Committee

رئيس الهيئة التحضيرية

الاستاذ الدكتور منير سالم طه

Prof. Dr. Muneer salim TAHA

مساعد رئيس جامعة الموصل للشؤون العلمية

Vice-president for Scientific Affairs of the University of Mosul

Iraq - العراق

General Secretary

الأمين العام للمؤتمر

أ. د. عبد الكريم دهش علي

Prof. Dr. Abdulkareem Dash ALI

جامعة تكريت

Tikrit University

Iraq - العراق

الرؤساء الفخريون
Honorary Committee

PROF. DR. WAAD MAHMOOD RAOOF

RECTOR OF TIKRIT UNIVERSITY

- Iraq

PROF. DR. ALYAA A. ALI AL–ATTAR

Rector of Northern Technical University

- Iraq

PROF. DR. TARIQ HAFDHI ABBD TAWFEEQ

President of the University of Al–Farhidi

- Iraq

PROF. DR. MUNEER SALIM TAHA

Vice Rector of Al–Iraqia University for Scientific Affairs

- Iraq

الهيئة الاستشارية
Consultative Committee

Prof. Dr. Ebtehag Zeki Sulyman Al Halim
University of Mosul
Iraq

Prof. Dr. Nezar Husein Ata Samarah
Jordan university of Science and Technology -Jordan

Dr. Osman TÜRK
Harran University
Türkiye

Prof. Dr. Hayajneh, Firas Mahmoud Faleh
Free University, Berlin-Germany
Jordan

Dr. Bader AL-AİFAN
Kuwait University
Kuwait

Dr. Nabil Mohie Abdel–Hamid ALY
Kafrelsheikh University
Egypt

Hussein Ali Mohammed AL_Ukaily
University of Wasit
Iraq

الهيئة التحضيرية
Organizing Committee

Prof. Dr. Lubna Abdulazeem Majeed AL-Bayati
University of Babylon
Iraq

Prof. Dr. Nihad Abdul-Lateef Ali
Al-Qasim Green UniversityTechnology -Jordan
Iraq

Prof. Dr. Mahmood Ahmad Hamood
University of Mosul
Iraq

Prof Dr Najwa Ibrahim Al-Barhawee
University of Mosul
Iraq

Dr. Esraa Habeeb Khaleel
Al-Qasim Green UniversityTechnology -Jordan
Iraq

Assist. Prof. Jalil Talab ABDULLA
Wasit University
Iraq

Assist. Prof. Dr. Methaq Abd Muslim GUDA
University of Kufa
Iraq

Lec.Dr. Hadeel Salih Mahdi
University of Misan
Iraq

Lect. Dr. Bassim Kareem Mihsin
General Directorate of Education in Karbala
Iraq

Dr. Haleemah Jaber MOHAMMED
Uruk university
Iraq

Dr. Riyam Adnan Hammudi Al inizi
College of Medicine, Wasit University
Iraq

Dr. Ihab Qays Ali Aldalawi
Ibn Sina university for medical and pharmaceutical sciences
Iraq

Assist. Prof. Iman radha JASIM
University of Mosul
Iraq

Assistant. prof .Dr. Rusul Alabada
Al-Muthanna university
Iraq

Dr. Thuraya A. abdulhussain
Al-Turath University
Iraq

الهيئة العلمية

Prof. Dr. Israa Abdul Razzaq Majed Al-Dobaissi
University of Baghdad
Iraq

Prof. Dr. Nawras Abdelah Alwan
Basrah University
Iraq

Prof. Dr. Baida Muhsen Ahmed
Mustansiriyah University
Iraq

Assist. Prof. Dr. Alaa Yaseen Taha Taqa
University of Mosul
Iraq

Assist. Prof. Dr. Rasha jawad kadhim
University of Sumer
Iraq

Assist. Prof. Dr. Fatima Rammadan ABDUL
Mustansiriyah University
Iraq

Assist. Prof. Dr. Ali faisal alsaad
Southern Technical University
Iraq

Assist. Prof. Dr. Intisar Ghanim Taha
Damascus University
Syria

Assist. Prof. Dr. Nihad Taha Mohammed JADDOA
University of Baghdad
Iraq

Assist . Prof . Dr. Ielaf O Abdul Majjed
University of Mosul
Iraq

Assoc. Prof. Dr. Eda M. A. Alshailabi
Omar Almukhtar University
LIBYA

Assist. Prof. Dr. Raghad Mukdad Mahmood AL.Hamdani
Tikrit University
Iraq

Lect. Dr. Sabah Noori HAMMOODİ
AShur University Collage
Iraq

Lect. Dr. Hadeel Waleed Abdulmalek AlJirjees
Baghdad University
Iraq

Lect. Dr. Shayma Muhsen Ahmad
Al-Nahrain University
Iraq

Lect. Dr. Eslah shakir rajab
Al-Karkh University of Science
Iraq

Lect. Dr. Aseel younis Khalaf Alnaimy
University of Babylon
Iraq

Lect. Dr. Mohammed Ali Hassan albeayaty
Al-Karkh University of Science
Iraq

Dr. Muslim Muhsin ALI
University of Missouri
USA

Dr. May Ahmed Fakhry Farhat Mousa
Alexandria University
Egypt

Dr. Abeer Saleem AbduKreem Almamury
University of Babylon
Iraq

Dr. Husam R. ABED
Ministry of Education
Iraq

Dr. Raja'a Al-Naimi
University of Petra
Jordan

Dr. Batool Abd Al Ameer Baqer ALSAFAR
Al Mustansiriyah University
Iraq

Dr. Nisreen SULAYMAN
Damascus University
Syrian

Dr. Nagwa mohammed mohammed elmobark
Egypt

Dr. Hind Husaam Al-Deen mohammed
University of Mosul
Iraq

Lect. Saja zubair aldhaif
University of Misan
Iraq

Assist. Lect. Mahmood Hameed Alsafi
University of Al-Qadisiyah
Iraq

Assist. Prof. Hanan Sami Nouri Alqutachi
University of Mosul
Iraq

Dr. Rayan Yousif YAcob Al-Khayat
UNIVERSITY OF MOSUL
Iraq

Dr. Shatha Hizem SHAKER
Tikrit University
Iraq

Dr.Ali farhan hashoosh
Misan University
Iraq

Lect. Dr. Rami Ali Taki Altameemi
South Dakota University Stat
United States

Dr. Wala Gazey Mahmood Dizayee
Salahaddin university
Erbil

DR.MOHAMMED SHAREEF MOHAMMED
Salahaddin university
Erbil

الهيئة العلمية

Prof. Dr. Sundus Nsaif Abed Alhuchaimi
University of Kufa
Iraq

Assoc. Prof. Dr.Osama Abd Alkareem Alhelu

Assist. Prof. Dr. Liqaa Zeki Hummady
University of Baghdad
Iraq

Dr. Saeed Jebor Hemza
Wasit University
Iraq

Assist. Prof. Dr. Zina Bakir Al-Hilli
Al-Qasim Green University
Iraq

Wurood Hantoosh Neamah
University of Basrah
Iraq

Assist. Prof. Dr. Najat Jalil Noon
Ministry of Education
Iraq

Assist. Prof. Aseel Amer Hassan
UUniversity of baghdad
Iraq

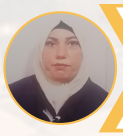

Lect. Dr. Hind Abdulrazzaq Mohammed Ali
University of Technology
Iraq

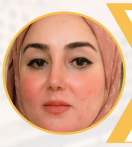

Lect Marwah Hussein Abdulsattar
Middle Technical University
Iraq

Lect. Dr. shahbaa fayadh bdewi
University of Anbar
Iraq

Dr. FOUZIA Youcef
University of Kasdi Merbah Ouargla
Algeria

Dr. Mutasim Ali Mohamed ELAGAB
Gezera University
Sudan

لجنة الاستقبال

Lect. Zainab Ismail abdulla
Northern Technical University
Iraq

Lect. Zianh Tareq Dahham
University of Mosul
Iraq

Lect. Shaymaa Alhayali
University of Mosul
Iraq

Lect. Zena Ez. Dallalbashi
Northern Technical University
Iraq

Assist. Lect. Safwan Jasim Sultan
University of Mosul
Iraq

INDEX

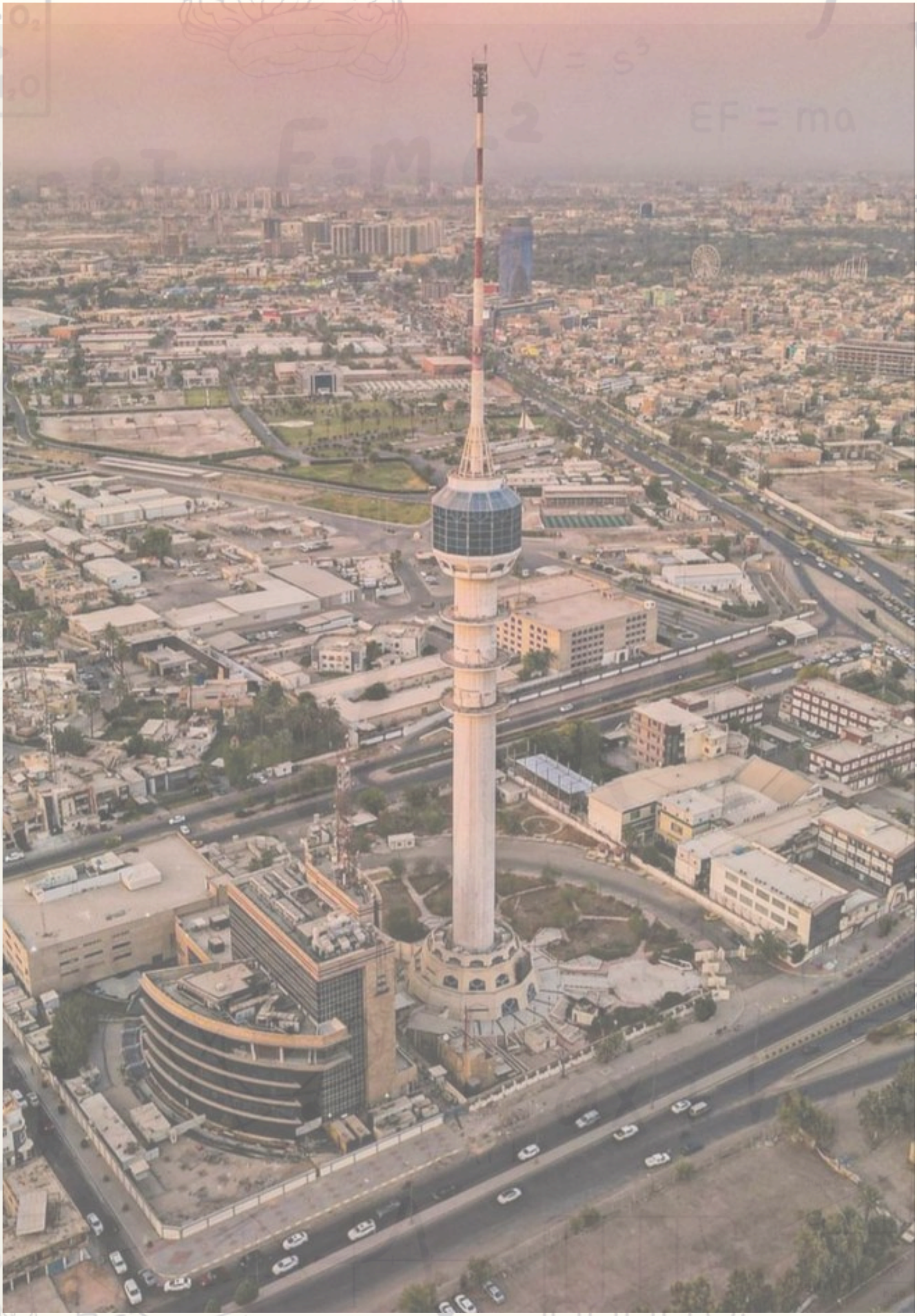

Antileishmanial Effects of Multi-Walled Carbon Nanotubes and Lactobacillus Acidophilus Cell-Free Supernatants: A Comparative Study on Leishmania Donovani and Leishmania Tropica

Mustafa Attiyah Hadid [1]

Ahmed Abd Temur [2]

Ibrahim Abdulkareem Sabri [3]

Zainab W. Abdulameer [4]

Abstract:

MTT assay was used to evaluate antiparasitic effect of agents after preparing 4 concentrations (12.5, 25, 50, and 75 µg/ml)for each of multi-walled carbon nanotubes (MWCNTs), *Lactobacillus acidophilus* cell free supernatant (CFS), a combination of multi-walled carbon nanotubes and *Lactobacillus acidophilus* cell free supernatant (MWCNT+CFS), and pentostam as reference drug. Results showed that all treatments have antileishmanial impact when compared to untreated group. Most effective treatments were belonging to CFS against both parasites followed by their combinations with MWCNT. There was no synergistic impact of the combination compared to the individual treatments. In conclusion, CFS alone has the most antileishmanial impact and it is more potent than its combination with nanomaterials, while MWCNT showed less antileishmanial effect although still considerable compared to untreated group.

Keyword: *Antileishmanial, Cell viability, CFS, Lactobacillus, Leishmania donovani, Leishmania tropica, Multiwalled carbon nanotubes, Nanoparticles*.

http://dx.doi.org/10.47832/RimarCongress07-1

[1] Researcher. College of Sciences, Al-Nahrain University, Iraq hadid.m.a@nahrainuniv.edu.iq

[2] Researcher. College of Sciences, Al-Nahrain University, Iraq ahmed.abed@nahrainuniv.edu.iq

[3] Researcher. College of Sciences, Al-Nahrain University, Iraq ibrahim.abdulkareem@nahrainuniv.edu.iq

[4] Researcher. Biotechnology Research Center, Al-Nahrain University, Iraq zainab.walid@nahrainuniv.edu.iq

Introduction

Leishmaniasis is a neglected tropical illness that has been threatening the world for more than a century. Parasites belonging to the genus *Leishmania* are the cause of the disease. The parasite manifests in three ways: visceral leishmaniasis, cutaneous leishmaniasis, and mucocutaneous leishmaniasis (Sasidharan & Saudagar, 2023). Visceral leishmaniasis is the most fatal form among the three, caused by *Leishmania donovani* (Sasidharan et al., 2019). *Leishmania* has two life stages: the amastigote, which has round to oval bodies and is only found in the macrophages of infected vertebrate hosts, and the promastigote, which is motile and has a single anterior flagellum and is found in the gut of sand flies (Singh, 2006; Ul Bari & Rahman, 2008). The disease is transmitted among the host via the bite of a Phlebotomus sandfly. Between 70,000 and 1 million cases are reported globally, while 26,000 to 65,000 people die from the disease each year (Harrison & Atala, 2007; Rathinavel et al., 2021). Amphotericin B liposomal formulation is still the first line of treatment, despite the fact that several medications have been developed to date to prevent the condition. These medications have a number of disadvantages, including high toxicity, organ failures, non-specificity, and lack of economic viability (Sasidharan & Saudagar, 2023). Strong synthesis techniques are enabling the rapidly developing field of nanobiotechnology to make significant advances (Sasidharan & Saudagar, 2020). Researchers are interested in nanoscale particles because of their many biotechnological uses (Sasidharan & Saudagar, 2021, 2022). In the twenty-first century, carbon nanotubes (CNTs) have gained interest due to their potential uses in biosensors, electronics, tissue engineering, gene therapy, and neuro-engineering (Sasidharan & Saudagar, 2023). They fall into one of two categories: single-walled carbon nanotubes (CNTs) or multiple-walled CNTs (MWCNTs). CNTs composition, surface modification, target microbes, and reaction environment all affect how antimicrobial they are (Wang & Zhang, 2011). In addition to the physical process of biologically isolating microbial cells from their supportive environment, antimicrobial mechanisms of CNTs depend on the invasion of the microbial cell wall or membrane and the development of structural damages (Azizi-Lalabadi et al., 2020).

The advantages of CFS have been shown, in addition to the usage of probiotic microbes. For example, *in vitro*, the CFS of *Lactobacillus* species showed 100% antiparasitic activity against *Toxocara canis* (Walcher et al., 2023).The primary metabolites found in the CFS of bacteria belonging to the species *Lactobacillus* are organic acids, particularly lactic acid, acetic acid, proteins, and hydrogen peroxide (H_2O_2) (Abdul-Rahim et al., 2021; Belguesmia et al., 2020). The primary functions of lactic and acetic acids include lowering pH, regulating IL8, enhancing the host immune response, and inhibiting the development of pathogen resistance (Netto de Oliveira da Cunha et al., 2024).

This study was aimed to test the antiparasitic activity of MWCNTs, CFS of *L. acidophilus*, and their combinations against *L. donovani* and *L. tropica* as well as comparing the most antiparasitic effect on both parasites.

Materials and methods

Cell-free supernatant preparation

Lactobacillus acidophilus isolate was generously provided by Department of Biology/College of Science/University of Baghdad. The probiotic activated twice by subculturing the stock solution in De Man, Rogosa, and Sharpe (MRS) broth (Oxoid, UK) and incubated anaerobically at 37 ˚C for 24 hours.

To prepare cell-free supernatant (CFS), 120 ml of MRS broth with 1x108 CFU/ml of 24 h grown *L. acidophilus* culture was incubated anaerobically at 37 ˚C, centrifuged at 4000 rpm for 15 m, and filtered through 0.22 µm pore-size filter papers (Microlab, UK) before lyophilising and storing at -20 ˚C (Hadid et al., 2025).

Functionalization of multi-walled carbon nanotubes (MWCNT)

A combination of 25% HNO_3 and 75% H_2SO_4 was used to treat 0.15 g of raw MWCNTs (SkySpring Nanomaterials, USA) in a flask. For 50 minutes at 37 °C, the raw material and acids were ultrasonically treated in the ultrasound bath. After that, the mixture was diluted with 40 ml of DI water using a 0.22 mm polypropylene membrane in a vacuum-filtered system. Next, 100% H_2O_2 was used in place of the solvent, and the same process was repeated by treating with H_2O_2 in a mild way. The particles were cleaned with deionised water until the filter's pH was about 7, and they were then dried in a furnace set between 170 and 200°C for 24 hours, producing functionalised MWCNT-COOH (MWCNTCOOH) (Ahmed, 2019)

Parasite Culture

The parasites *L. donovani* and *L. tropica* were graciously donated by the Biotechnology Research Centre at Al-Nahrain University. The promastigotes were cultured in 199 medium with 50 µg/ml penicillin and 10% HI-FBS at 26°C (Zghair et al., 2016).

MTT assay

Four concentrations (2.5, 25, 50and 75 µg/ml) of each of MWCNT, CFS, MWCNT+CFS, and pentostam drug were prepared and dispersed in a flat-bottom 96-well microtiter plate containing *L. donovani* and *L. tropica* promastigotes (2 x 10^5 parasites/well) and incubated at 25˚C (Zghair et al., 2016). The combinations of MWCNT+CFS were made by adding MWCNT and CFS in 1:1 ratio for each concentration. The microtiter plate was incubated at 25˚C for 24 hrs. After incubation, 10 µl of MTT solution was applied to each well. The microtiter plate was incubated for 4 hours at 25˚C. To solubilise the formazan crystals, remove the medium and add 100µl of DMSO solution. After gently stirring the microtiter plate, it was left for fifteen minutes. The ELISA reader was used to measure the optical absorbance of these plates at 570 nm.

The cell viability was measured by the formula below:

$$\text{Viability (\%)} = (\text{Mean OD}_{\text{sample}} - \text{Mean OD}_{\text{blank}}) / (\text{Mean OD}_{\text{control}} - \text{Mean OD}_{\text{blank}}) \times 100$$

Statistical analysis

The data was analysed using ANOVA and Tukey's/Dunnett's multiple comparison tests, with a significance level of p-value < 0.05. These analyses were carried out with GraphPad Prism version 8.4.3.

Results

The IC_{50} results revealed varied susceptibility of *L. donovani* and *L. tropica* to the investigated treatments (Figures 1 and 2). MWCNTs had modest activity against *L. donovani* (IC_{50} = 24.14 µg/mL, R^2 = 0.84), while CFS had a significantly larger effect (IC_{50} = 5.87 µg/mL, R^2 = 0.94). The combination of MWCNTs with CFS resulted in the same inhibitory concentration (IC_{50} = 5.87 µg/mL, R^2 = 0.94), indicating no additional additive effect compared to CFS alone. Pentostam, the reference drug, showed the highest potency (IC_{50} = 3.35 µg/mL, R^2 = 0.87).

MWCNTs showed slightly higher activity against *L. tropica* compared to *L. donovani* (IC_{50} = 19.53 µg/mL, R^2 = 0.85). CFS showed substantial inhibition (IC_{50} = 4.32 µg/mL, R^2 = 0.92). However, unlike *L. donovani*, the combination of MWCNTs + CFS demonstrated an intermediate impact (IC_{50} = 12.43 µg/mL, R^2 = 0.87), which was weaker than CFS alone. Pentostam maintained its effectiveness (IC_{50} = 3.97 µg/mL, R^2 = 0.91). Overall, these findings show that CFS outperforms MWCNTs in both *Leishmania* species, with Pentostam serving as the most effective control. Interestingly, while the combination did not outperform CFS alone in *L. donovani*, it had a lower efficacy in *L. tropica*, indicating species-specific interactions.

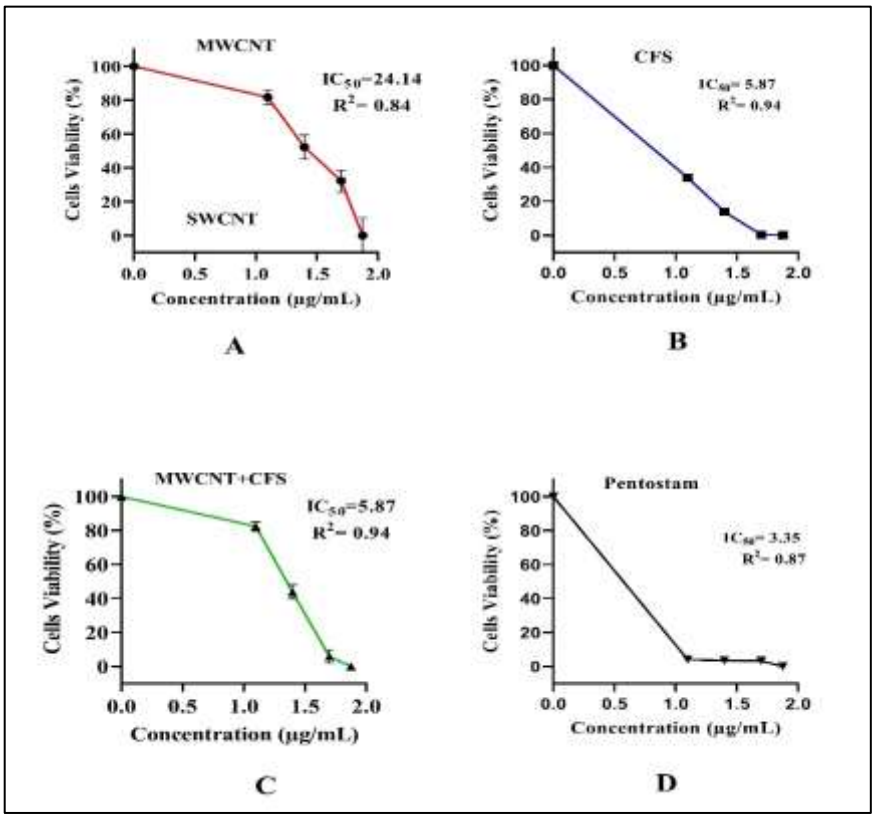

Figure 1 Antileishmanial impact of MWCNTs, CFS of *L. acidophilus* and their combinations against *Leishmania donovani*

Our results showed that all treatments were significant in reducing the parasite viability of both *L. donovani and L. tropica* when compared to untreated group (Figure 3). Also, the impact of CFS alone was higher against both parasites than nanomaterials alone nor their combination with CFS which is in line with IC_{50} results. It is noteworthy that CFS treatment was more potent than pentostam against *L. donovani* and was as similar in potency as pentostam against *L. tropica*.

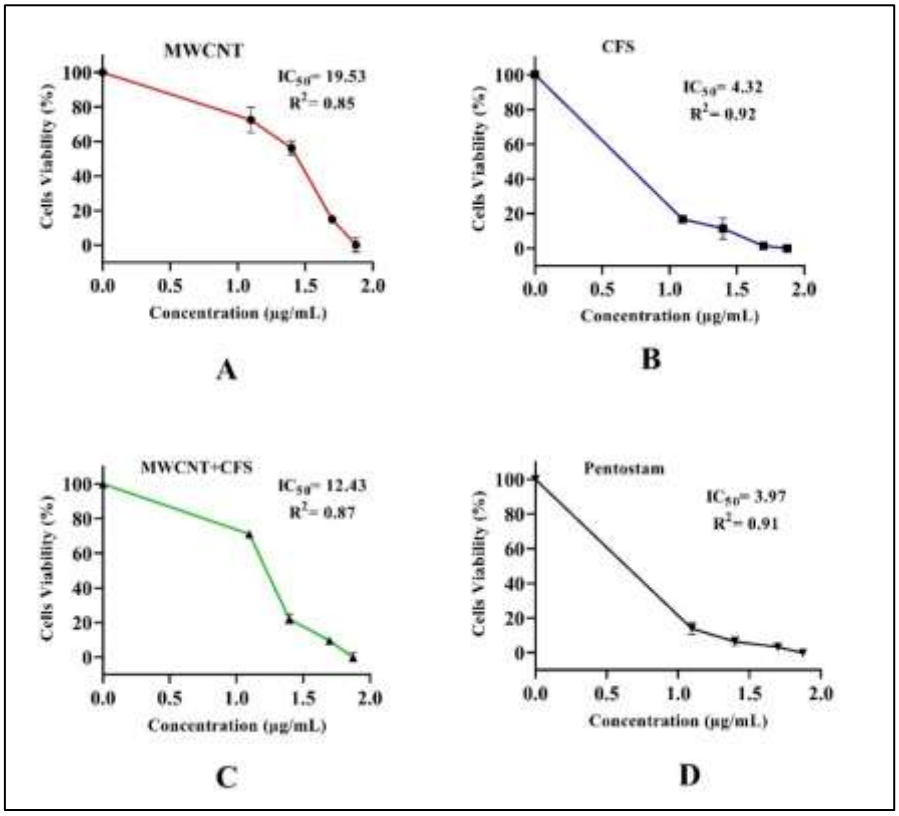

Figure 2 Antileishmanial impact of MWCNTs, CFS of L. acidophilus and their combinations against Leishmania tropica

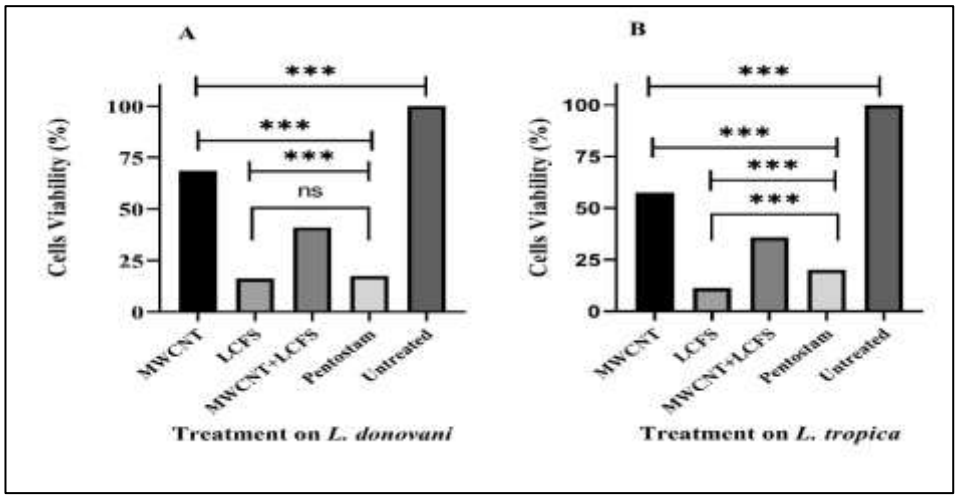

Figure 3 Antileishmanial effects of MWCNTs, L. acidophilus CFS, and their combination on (A) Leishmania donovani and (B) Leishmania tropica, with Pentostam included as a reference control

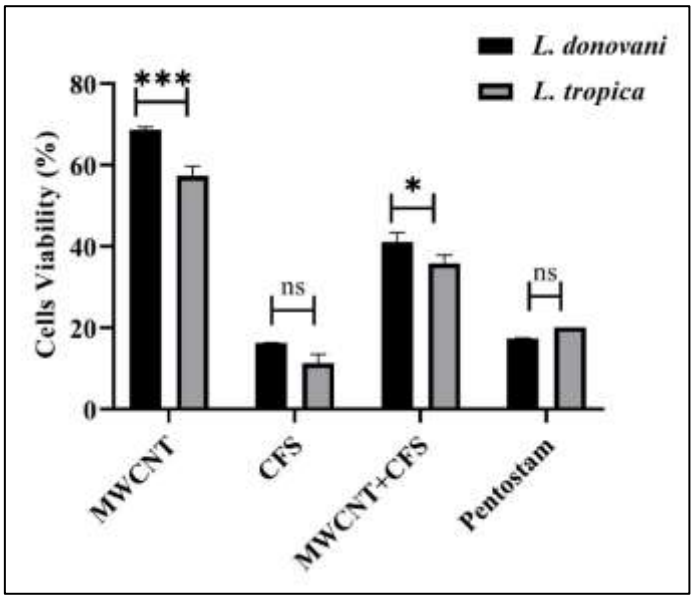

Figure 4 A comparison between the antileishmanial effect of MWCNTs, L. acidophilus CFS, and their combination toward L. donovani and L. tropica

When a comparison made between *L. donovani* and *L. tropica* results demonstrated that MWCNT was more effective against *L. tropica* than *L. donovani* similar findings obtained from MWCNT+CFS (Figure 5). On the other hand, there were no significant differences between *L. donovani* and *L. tropica* in the treatment of CFS alone and pentostam.

Discussions

This study examined the antileishmanial properties of L. acidophilus cell-free supernatant (CFS), multi-walled carbon nanotubes (MWCNTs), and their combination against *L. tropica* and *L. donovani*. The findings showed clear species-specific reactions, with pentostam acting as the most successful reference control and CFS continuously exhibiting higher activity than MWCNTs.

With IC_{50} values that were comparable to pentostam, CFS demonstrated impressive inhibitory effects on both *L. donovani* and *L. tropica*. Probiotic-derived metabolites have been shown in recent research to have antiparasitic potential, producing bacteriocins, organic acids, and biosurfactants with direct antiparasitic activity. The way probiotics work is by secreting organic acids like lactic, butyric, and acetic acid as well as antibacterial substances like bacteriocins that may have antiparasitic properties (Chiodo et al., 2010; Hernández-González et al., 2021; LeBlanc et al., 2017).

Our results further highlight the potential of probiotics and their metabolites as supplemental or alternative approaches to the treatment of leishmaniasis. It's interesting to note that CFS activity was much stronger in *L. donovani* than in pentostam, suggesting that it might be better than traditional medications in some circumstances.

On the other hand, the antiparasitic effects of MWCNTs were mild but noteworthy. Despite generally being less effective than CFS, MWCNTs demonstrated their potential as antiparasitic drugs by significantly reducing parasite viability as compared to untreated groups. In *L. donovani*, for example, parasite inhibition was close to 40%, but in *L. tropica*, it

was over 50%. According to this, carbon nanotubes may have significant antiparasitic effects. They may work by disrupting membranes, inducing oxidative stress, and interfering with parasite metabolic processes (Demir, 2022). A study showed that amphotericin B functionalised carbon nanotubes had no discernible deleterious effects and were far more effective against leishmaniasis than amphotericin B (Foldvari & Bagonluri, 2008). These findings matched with earlier research that shown the effectiveness of CNTs against *Leishmania* species *in vitro* (Mohebali et al., 2009).

MWCNTs have significant potential as an antiparasitic agent, even if CFS seems more effective and secure. This is especially true if future studies concentrate on functionalisation or tailored delivery methods to increase selectivity.

The effects of combining the two agents varied according on the type of parasite. The combination of MWCNT and CFS in *L. donovani* had an effect that was comparable to that of CFS alone, indicating no additive or synergistic advantage. The combination, however, was less efficient in *L. tropica* than CFS alone, possibly as a result of surface interference between the nanomaterials and the active metabolites in the supernatant.

These results demonstrate the complex nature of interactions between nanomaterials and biomolecules and the necessity of carefully assessing combinations rather than relying on the assumption that they will increase efficacy. In this regard (Auría-Soro et al., 2019) mentioned that nanoparticles can behave differently depending on the surrounding medium conditions (pH, ionic strength, organic matter, etc.), which may lead to aggregation or interaction with other biomolecules. Such changes can create heterogeneous morphologies and reduce stability or biocompatibility.

MWCNTs and the MWCNT + CFS combination were dramatically more effective against *L. tropica* than *L. donovani*; however, there was no difference in CFS or pentostam activity between the two species. This implies that the susceptibility of *Leishmania* spp. to nanomaterial-based therapies may be strain- or species-dependent.

Conclusions

L. acidophilus cell-free supernatants (CFS) exhibited strong antileishmanial activity against *L. donovani* and *L. tropica*, in some cases comparable to the reference drug pentostam. MWCNTs established considerable inhibitory effects as compared to untreated controls, showing their antiparasitic potential even though they were not as effective as CFS. MWCNTs and CFS produced species-specific results, with *L. donovani* showing no extra antiparasitic impact and *L. tropica* showing decreased effect. These results show that CFS is a promising natural treatment option, but they also imply that more optimisation of nanomaterials is necessary to maximise their antileishmanial potential.

References:

Abdul-Rahim, O., Wu, Q., Price, T. K., Pistone, G., Diebel, K., Bugni, T. S., & Wolfe, A. J. (2021). Phenyl-lactic acid is an active ingredient in bactericidal supernatants of lactobacillus crispatus. Journal of Bacteriology, 203(19). https://doi.org/10.1128/JB.00360-21

Ahmed, A. S. (2019). Functionalization of single and multi-walled carbon nanotubes by chemical treatment. Iraqi Journal of Physics, 16(39), 55–63. https://doi.org/10.30723/ijp.v16i39.103

Auría-Soro, C., Nesma, T., Juanes-Velasco, P., Landeira-Viñuela, A., Fidalgo-Gomez, H., Acebes-Fernandez, V., Gongora, R., Parra, M. J. A., Manzano-Roman, R., & Fuentes, M. (2019). Interactions of nanoparticles and biosystems: Microenvironment of nanoparticles and biomolecules in nanomedicine. In Nanomaterials (Vol. 9, Issue 10, p. 1365). Multidisciplinary Digital Publishing Institute. https://doi.org/10.3390/nano9101365

Azizi-Lalabadi, M., Hashemi, H., Feng, J., & Jafari, S. M. (2020). Carbon nanomaterials against pathogens; the antimicrobial activity of carbon nanotubes, graphene/graphene oxide, fullerenes, and their nanocomposites. Advances in Colloid and Interface Science, 284, 102250. https://doi.org/10.1016/J.CIS.2020.102250

Belguesmia, Y., Hazime, N., Kempf, I., Boukherroub, R., & Drider, D. (2020). New bacteriocins from lacticaseibacillus paracasei cncm i-5369 adsorbed on alginate nanoparticles are very active against escherichia coli. International Journal of Molecular Sciences, 21(22), 1–15. https://doi.org/10.3390/ijms21228654

Chiodo, P. G., Sparo, M. D., Pezzani, B. C., Minvielle, M. C., & Basualdo, J. A. (2010). In vitro and in vivo effects of Enterococcus faecalis CECT7121 on Toxocara canis. Memorias Do Instituto Oswaldo Cruz, 105(5), 615–620. https://doi.org/10.1590/S0074-02762010000500003

Demir, E. (2022). Mechanisms and biological impacts of graphene and multi-walled carbon nanotubes on Drosophila melanogaster: Oxidative stress, genotoxic damage, phenotypic variations, locomotor behavior, parasitoid resistance, and cellular immune response. Journal of Applied Toxicology, 42(3), 450–474. https://doi.org/10.1002/jat.4232

Foldvari, M., & Bagonluri, M. (2008). Carbon nanotubes as functional excipients for nanomedicines: II. Drug delivery and biocompatibility issues. In Nanomedicine: Nanotechnology, Biology, and Medicine (Vol. 4, Issue 3, pp. 183–200). Elsevier. https://doi.org/10.1016/j.nano.2008.04.003

Hadid, M. A., Hasan, A. F., Al-Halbosiy, M. F., Al-Maliki, N. S., Al-Shaibani, A. B., Mohammed, S. A., & El-Wahsh, H. M. (2025). Cytotoxicity and Apoptosis Induction of

Lactobacillus acidophilus Cell-free Supernatant against Human Colon Carcinoma Cell Line. Agricultural Reviews, Of. https://doi.org/10.18805/ag.rf-383

Harrison, B. S., & Atala, A. (2007). Carbon nanotube applications for tissue engineering. In Biomaterials (Vol. 28, Issue 2, pp. 344–353). Elsevier. https://doi.org/10.1016/j.biomaterials.2006.07.044

Hernández-González, J. C., Martínez-Tapia, A., Lazcano-Hernández, G., García-Pérez, B. E., & Castrejón-Jiménez, N. S. (2021). Bacteriocins from lactic acid bacteria. A powerful alternative as antimicrobials, probiotics, and immunomodulators in veterinary medicine. In Animals (Vol. 11, Issue 4). Animals (Basel). https://doi.org/10.3390/ani11040979

LeBlanc, J. G., Chain, F., Martín, R., Bermúdez-Humarán, L. G., Courau, S., & Langella, P. (2017). Beneficial effects on host energy metabolism of short-chain fatty acids and vitamins produced by commensal and probiotic bacteria. In Microbial Cell Factories (Vol. 16, Issue 1). Microb Cell Fact. https://doi.org/10.1186/s12934-017-0691-z

Mohebali, M., Rezayat, M. M., Gilani, K., Sarkar, S., Akhoundi, B., Esmaeili, J., Satvat, T., Elikaee, S., Charehdar, S., & Hooshyar, H. (2009). Nanosilver in the treatment of localized cutaneous leishmaniasis caused by Leishmania major (MRHO/IR/75/ER): An in vitro and in vivo study. Daru, 17(4), 285–289. http://daru.tums.ac.ir/index.php/daru/article/view/557.pdf

Netto de Oliveira da Cunha, C., Rodeghiero Collares, S., Carvalho Rodrigues, D., Walcher, D. L., Quintana de Moura, M., Rodrigues Martins, L. H., Baracy Klafke, G., de Oliveira Arias, J. L., Carapelli, R., do Santos Espinelli Junior, J. B., Scaini, C. J., & Farias da Costa de Avila, L. (2024). The larvicidal effect of the supernatant of Lactobacillus acidophilus ATCC 4356 on Toxocara canis. Experimental Parasitology, 258, 108720. https://doi.org/10.1016/j.exppara.2024.108720

Rathinavel, S., Priyadharshini, K., & Panda, D. (2021). A review on carbon nanotube: An overview of synthesis, properties, functionalization, characterization, and the application. In Materials Science and Engineering: B (Vol. 268, p. 115095). Elsevier. https://doi.org/10.1016/j.mseb.2021.115095

Sasidharan, S., Raj, S., Sonawane, S., Sonawane, S., Pinjari, D., Pandit, A. B., & Saudagar, P. (2019). Nanomaterial synthesis: Chemical and biological route and applications. In Nanomaterials Synthesis: Design, Fabrication and Applications (pp. 27–51). Elsevier. https://doi.org/10.1016/B978-0-12-815751-0.00002-X

Sasidharan, S., & Saudagar, P. (2020). Flavones reversibly inhibit Leishmania donovani tyrosine aminotransferase by binding to the catalytic pocket: An integrated in silico-in vitro approach. International Journal of Biological Macromolecules, 164, 2987–3004. https://doi.org/10.1016/j.ijbiomac.2020.08.107

Sasidharan, S., & Saudagar, P. (2021). Leishmaniasis: where are we and where are we heading? SpringerS Sasidharan, P SaudagarParasitology Research, 2021•Springer, 120(5), 1541–1554. https://doi.org/10.1007/S00436-021-07139-2

Sasidharan, S., & Saudagar, P. (2022). Gold and silver nanoparticles functionalized with 4',7-dihydroxyflavone exhibit activity against Leishmania donovani. Acta Tropica, 231, 106448. https://doi.org/10.1016/j.actatropica.2022.106448

Sasidharan, S., & Saudagar, P. (2023). 4′,7-dihydroxyflavone conjugated carbon nanotube formulation demonstrates improved efficacy against Leishmania parasite. Biochimica et Biophysica Acta - General Subjects, 1867(10), 130416. https://doi.org/10.1016/j.bbagen.2023.130416

Singh, S. (2006). New developments in diagnosis of leishmaniasis. In Indian Journal of Medical Research (Vol. 123, Issue 3, pp. 311–330). https://doi.org/10.5555/20063107904

Ul Bari, A., & Rahman, S. B. (2008). Cutaneous leishmaniasis: An overview of parasitology and host-parasite-vector inter relationship. In Journal of Pakistan Association of Dermatologists (Vol. 18, Issue 1, pp. 42–48). http://jpad.com.pk/index.php/jpad/article/view/564

Walcher, D. L., De Sousa, N. F. G. C., Rocha, L. S., Mattos, G. T., Klafke, G. B., Scaini, J. L. R., Berne, M. E. A., Avila, L. F. C., & Scaini, C. J. (2023). Larvicide Activity of Lactobacillus spp. and Saccharomyces boulardii Supernatants on Toxocara canis. Journal of Parasitology, 109(1), 15–19. https://doi.org/10.1645/20-161

Wang, F., & Zhang, K. (2011). Reduced graphene oxide-TiO2 nanocomposite with high photocatalystic activity for the degradation of rhodamine B. Journal of Molecular Catalysis A: Chemical, 345(1–2), 101–107. https://doi.org/10.1016/j.molcata.2011.05.026

Zghair, K. H., Saheb, E. J., & AL-Qadhi, B. N. (2016). Antiparasitic Effect of Carbonnanotubes on Leishmania donovani in vitro. Iraqi Journal of Science, 57(4B), 2641–2649. https://ijs.uobaghdad.edu.iq/index.php/eijs/article/view/6309

Antimicrobial Evaluation of Chemically Synthesized ZnO Nanoparticles Against Escherichia Coli

Akram A. Khalaf [1]

Furqan Majid Kadhum [2]

Diyar J. Hassan [3]

Tabarak A. Al-Mashhadani [4]

Abstract:

MTT assay was used to evaluate antiparasitic effect of agents after preparing 4 concentrations (12.5, 25, 50, This study investigates the antimicrobial activity of zinc oxide (ZnO) nanoparticles synthesized by chemical methods at concentration of 11.32×10^{-1} M against Escherichia coli (E. coli). The ZnO nanoparticles characterized by X-ray diffraction (XRD), Filed Emission Scanning Electron Microscopy (FE-SEM), and UV–visible spectroscopy to confirm their nanoscale size, morphology, and optical properties.

The results revealed a clear inhibition zone around ZnO nanoparticles, demonstrating significant antibacterial activity. Chemically synthesized ZnO nanoparticles show promising potential as effective antimicrobial agents against E. coli, suggesting their possible application in biomedical, pharmaceutical, and environmental fields.

Keywords: *Zinc Oxide Nanoparticles, Antibacterial Activity, Escherichia Coli, Biomedical Applications, Nanotechnology*.

http://dx.doi.org/10.47832/RimarCongress07-2

[1] Researcher. College of Science, AL-Karkh University of Science, Iraq akram.abdullah@kus.edu.iq

[2] Researcher. Al-Farabi University College, Baghdad, Iraq furqanmajid15@gmail.com

[3] Researcher. College of Pharmacy, University of Baghdad, Iraq diyar.j@copharm.uobaghdad.edu.iq

[4] Researcher. Institute of Laser for Postgraduate Studies, University of Baghdad, Iraq tabarak.amar1204a@sc.uobaghdad.edu.iq

Introduction

Nanotechnology's wide range of inventive uses in advanced textile manufacturing, food processing, medical diagnostics and therapeutics, and agricultural production have made it one of the most forward-thinking and quickly growing areas of contemporary scientific and technological research [1,2]. In order to define, optimize, and improve the structural and functional properties of both natural and artificial systems, this field uses extremely sophisticated approaches [3].

Materials that have innovative and significantly improved physicochemical and biological properties, as well as special phenomena and functionalities that are not present in their bulk equivalents, are the subject of the current investigation because of their nanoscale dimensions [4]. The surface-to-volume ratios of nanoparticles (NPs), which are generally between 1 and 100 nm in size, are significantly larger than those of macroscale materials [5–7]. These unique structural characteristics give nanoparticles remarkable physicochemical characteristics, which make them extremely important in a variety of applications, including the development of sophisticated biosensors and nanomedicine [8].

When metallic nanoparticles, such as silver (Ag), zinc oxide (ZnO), and titanium dioxide (TiO_2), are reduced to the nanoscale level, they can be engineered to exhibit tunable characteristics, including size, morphology, crystallinity, composition, and various physicochemical properties (chemical, mechanical, electrical, structural, morphological, and optical) [9]. For biomedical applications, this nanoscale alteration is essential because it permits special interactions with biological molecules and makes it easier for nanoparticles to enter cellular structures [8].Nanostructured materials' higher percentage of surface atoms improves their reactivity and interaction potential, which helps explain why bio nanotechnology and the basic and applied sciences are becoming more and more interested in them. Zinc oxide (ZnO), one of the metal oxide nanoparticles, has garnered a lot of scientific attention because of its remarkable antibacterial activity against a variety of bacterial species [10–15]. Comparative studies have demonstrated that when ZnO is produced at the nanoscale, it has strong antibacterial properties. ZnO nanoparticles start a variety of bactericidal processes when they come into contact with bacterial membranes or intracellular components [14,16].

ZnO nanoparticles' high toxicity to bacteria and compatibility with human cells have led to their growing application as antimicrobial agents in the food sector. Numerous studies have verified ZnO-NPs' biocompatibility and biosafety, showing that they are strong antibacterial agents without harming human cells [17–19]. The effectiveness of nanoparticles against bacteria is largely dependent on their high surface area-to-volume ratio [20]. More investigation into ZnO nanoparticles' antibacterial potential is crucial for developing global health solutions and battling microbial resistance because of their unique physicochemical properties [21].

Experimental

Escherichia coli were selected and ready for testing in the current bioactivity application. Escherichia coli were cultivated for a whole day in nutrient broth. After being incubated for the entire night, the isolates were diluted to the McFarland standard and 0.1 ml of a diluted bacterial culture was uniformly spread on Muller-Hinton agar plates.

Powdered ZnO nanoparticles were dissolved in deionized water to create solutions with concentrations of ZnO nanoparticles of 11.32×10^{-1} M, homogenized by a vortex mixer, and added to the plates. Growth inhibitory zone formation was examined following a final 24-hour incubation period at 37 °C.

Results and discussion

The XRD patterns of ZnO NPs are given as indicated in figure 1 in order to investigate the phase structure for the ZnO nanoparticles that were synthesized as powder. The ZnO nanoparticles' polycrystalline structure is revealed by the X-ray pattern, which shows 11 peaks at the following diffraction angles: 31.8° (100), 34.4° (002), 36.2° (101), 47.6° (102), 56.6° (110), 63.3° (103), 66.6° (200), 68.3° (112), 69.2° (004), 72.8° (201), and 77.2° (202). A hexagonal structure is mentioned in [22–23].

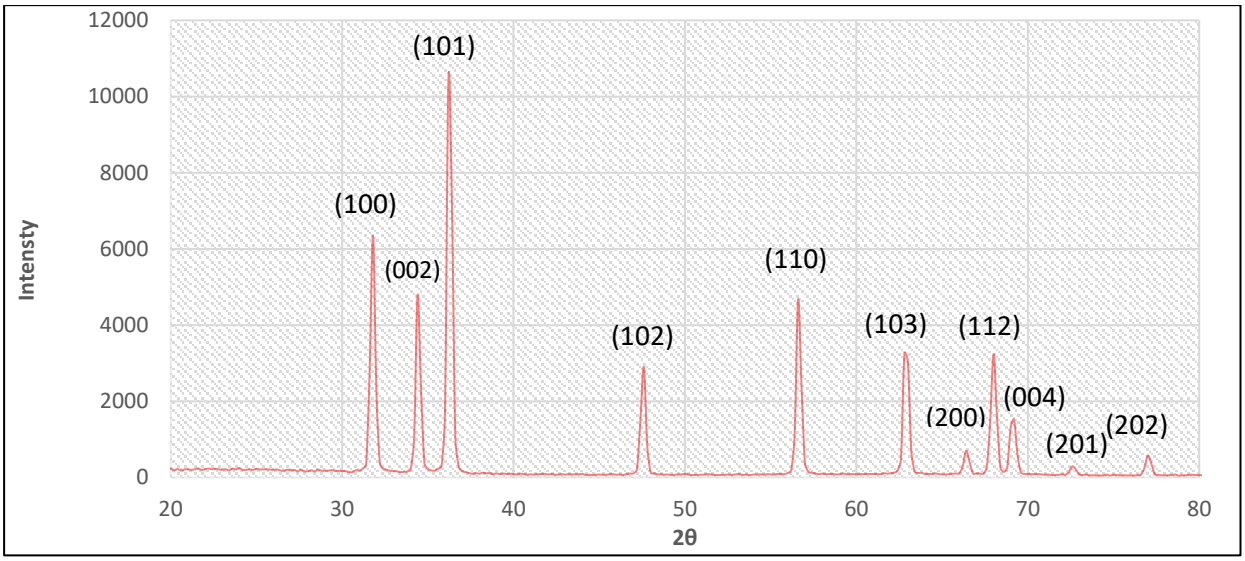

Figure 1: X-ray Diffraction of ZnO Nanoparticles

Field Emission- Scanning Electron Microscopy plays a crucial role in numerous applications and is a practical way to examine the structure of sample. Figure 2 shows FE-SEM pictures of ZnO nanoparticle, with the surface coated with equally distributed particles of different types (nanosheets, star shapes, and rods).

A uniform distribution of nanoparticles could be observed by analyzing the image in Figure 2. The distribution of particle sizes progressively shifts from smaller to larger aggregates. According to the particle size value determined by FE-SEM measurements, the size ranges from 26.23 to 379.3 nm at a concentration of 11.32×10^{-1} M. These results

corroborate the hypothesis that a particle of small size is obtained. Additionally, the image indicates the inclusion of some particle agglomerations [24].

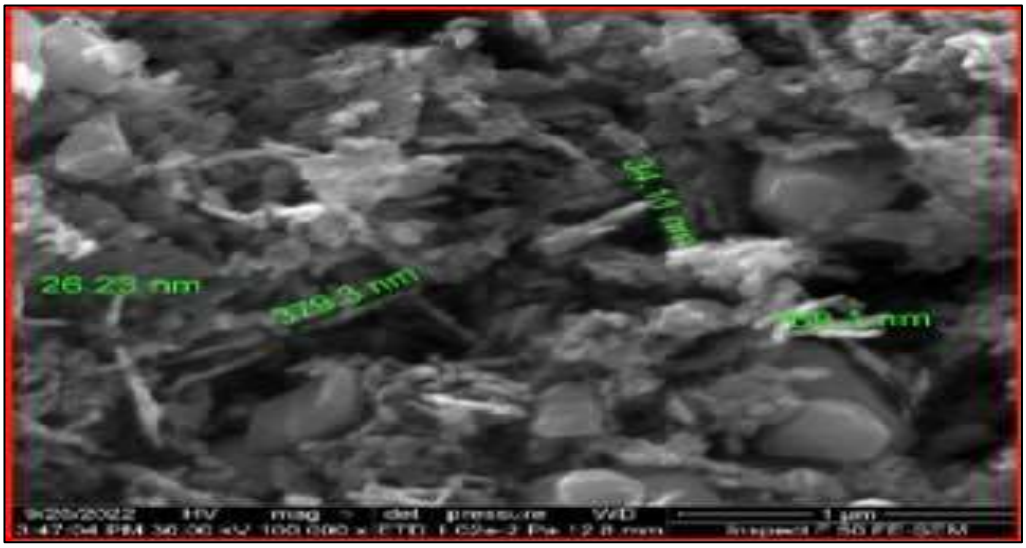

Figure 2: FE-SEM image of ZnO Nanoparticles.

Figure 3 exhibits the ZnO Nanoparticles solution's FTIR spectrum at a concentration of 11.32×10^{-1} M in the 400–4000 cm^{-1} wavenumber region. ZnO bond absorption is characterized by peaks at 559,670, and 813 cm^{-1}, which correspond to the hexagonal ZnO phase in XRD.

The O-H absorption is responsible for the peak at 3428 cm^{-1}. The absorption of C=C is responsible for the peak at 2359 cm^{-1}, while the range between 2907 and 2936 cm^{-1} is associated with C-H. The absorption of C=O is responsible for the peaks at 1659, 1458, and 1557 cm^{-1}, while C-N is linked to the peak at 1103 cm^{-1} [25].

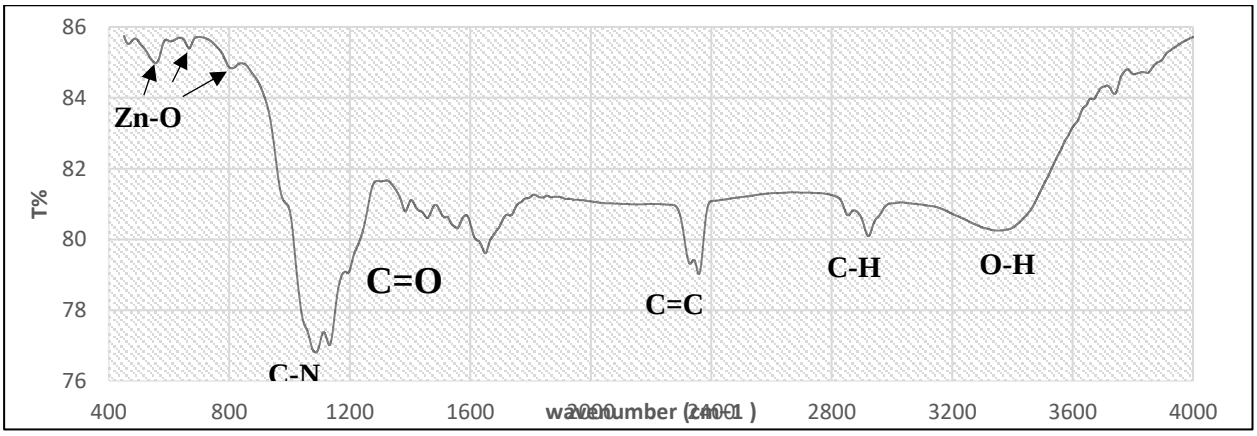

Figure 3: FTIR spectrum ZnO Nanoparticles .

In Figure (4), the Energy Dispersive X-ray (EDX) spectra of ZnO nanoparticles have been recorded and analyzed. The tables and figure indicate the final sample's elemental structure. The existence of oxygen and zinc atoms in the thin layers, which indicated the creation of thin films, was confirmed by the examined sample's EDX spectra. The final samples' weight percentages of carbon, oxygen, and zinc were determined to be 14.9%, 36.8%, and 48.2%, respectively.

Element	Atomic %	Atomic % Error	Weight %	Weight % Error
C	14.9	0.7	4.6	0.2
O	36.9	0.7	15.1	0.3
Zn	48.2	0.5	80.4	0.8

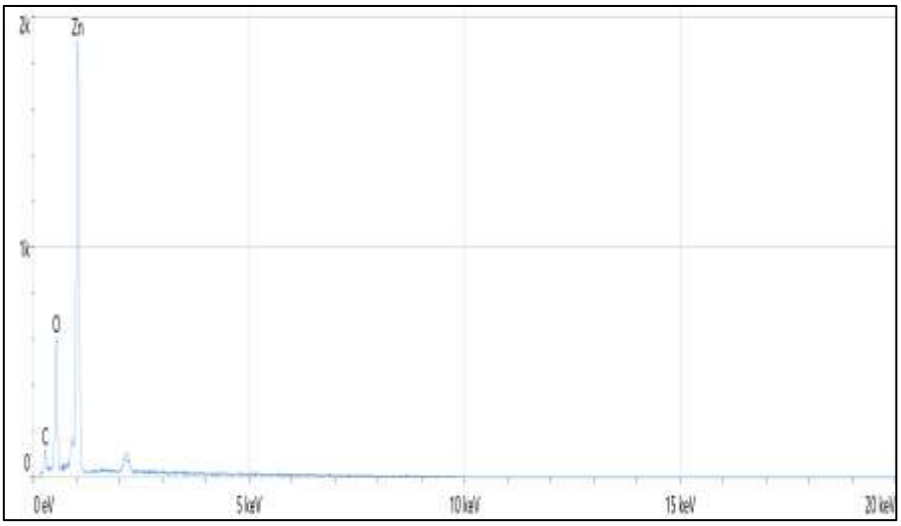

Figure 5: The EDX spectrum of ZnO Nanoparticles.

The absorbance of ZnO colloidal particles was measured, as shown in Figure (5). The peak was found to be in the 378–386 nm range, and the absorption in this area is caused by the development of zinc oxide nanoparticles [26].

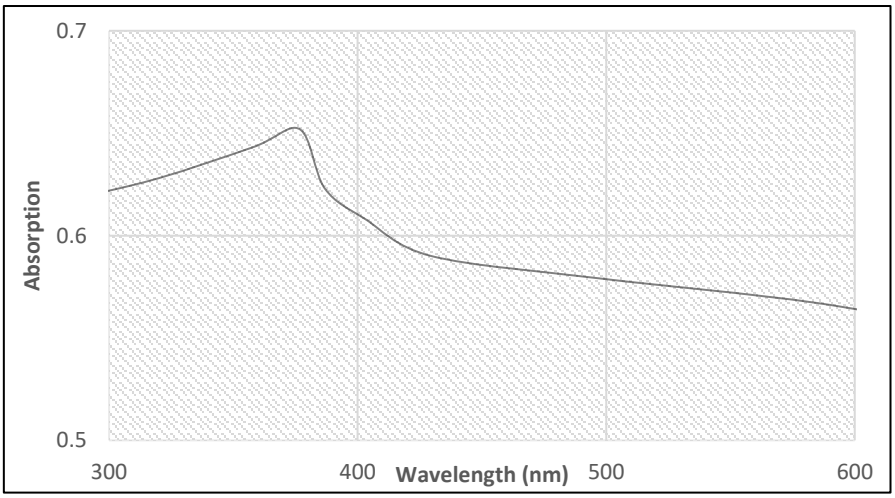

Figure 5: The absorption spectra of ZnO Nanoparticles .

Figure 6 shows Escherichia coli bacteria isolates before treatment and the antibacterial activity of ZnO nanoparticles against Escherichia coli. Heat-induced free radical production is linked to ZnO nanoparticle activity; when these radicals contact with the bacterial cell membrane, peroxidation results. Bacteria can be broken down and eliminated as a result of the oxidation of organic substances by the ensuing highly active oxygen molecules. The

findings demonstrated that the antibacterial properties of ZnO nanoparticles at 11.32×10^{-1} M were superior to those.

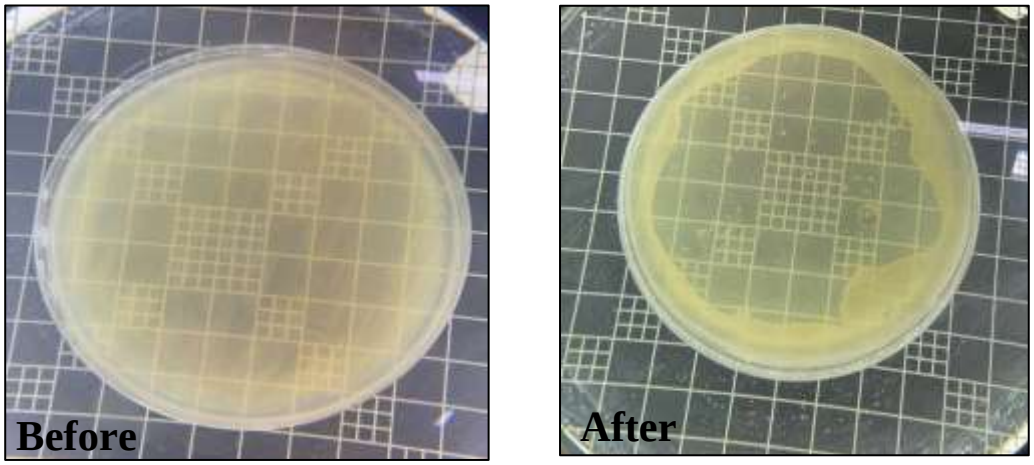

Figure 6: Before and after antibacterial activity of ZnO nanoparticles against Escherichia coli.

Conclusions

The results demonstrate that chemically produced ZnO NPs have a great deal of promise as strong antibacterial agents, especially when it comes to Gram-negative bacteria like E. coli. Therefore, in applications related to biomedicine, the environment, and food preservation, ZnO nanoparticles can be regarded as a promising substitute for traditional antibiotics. It is advised that more research be done to examine their cytotoxicity, biocompatibility, and functionality in intricate biological systems.

References:

Deshmukh, S. K., Kochar, M., Kaur, P., & Singh, P. P. (Eds.). (2023). *Nanotechnology in agriculture and environmental science*. CRC Press.

Al-Mashhadani, T. A., & Al-Maliki, F. J. (2022). Optimized characteristics of silver nanoparticles synthesized by chemical reduction and embedded in silica xerogels. *Iraqi Journal of Applied Physics, 18*(3).

Taha, S. M., & Manshad, A. K. (2025). Multifunctional Green Synthesized Hybrid Nanofluid System for Asphaltene Control and Crude Oil Conditioning: An Integrated Flow Assurance Solution. *Asia-Pacific Journal of Chemical Engineering*, e70097.

Du, A., Hua, L., Guo, Z., Jia, F., Xu, X., Wang, S., & Lu, Z. (2025). Nano-engineered fiber-based sensing frontiers: Revolutionizing on-site pesticide detection for global food-environment nexus challenges. *Coordination Chemistry Reviews*, *538*, 216710.

Sajid, M., & Płotka-Wasylka, J. (2020). Nanoparticles: Synthesis, characteristics, and applications in analytical and other sciences. *Microchemical Journal, 154,* 104623.

Abdel-Mageed, H. M., AbuelEzz, N. Z., Radwan, R. A., & Mohamed, S. A. (2021). Nanoparticles in nanomedicine: A comprehensive updated review on current status, challenges, and emerging opportunities. *Journal of Microencapsulation, 38*(6), 414-436.

Yameny, A. (2024). A comprehensive review on nanoparticles: Definition, preparation, characterization, types, and medical applications. *Journal of Medical and Life Sciences, 6*(4), 663-672.

Pushpalatha, C., Suresh, J., Gayathri, V. S., Sowmya, S. V., Augustine, D., Alamoudi, A., Zidane, B., Mohammad Albar, N. H., & Patil, S. (2022). Zinc oxide nanoparticles: A review on its applications in dentistry. *Frontiers in Bioengineering and Biotechnology, 10,* 917990.

Mashhadani, T. A., & Kadhim, F. J. (2023). Photoluminescence properties of silver-dysprosium co-doped silica obtained by sol–gel method. *Journal of Sol-Gel Science and Technology, 106*(2), 553-560.

Adams, C. P., Walker, K. A., Obare, S. O., & Docherty, K. M. (2014). Size-dependent antimicrobial effects of novel palladium nanoparticles. *PLOS ONE, 9*(1), e85981.

Kumarage, V., Siriwardane, I. W., Sandaruwan, C., Kandanapitiya, M. S., Kottegoda, N., & Jayewardenepura, G. (2022). Nanotechnology applications in biomaterials: A review. *Journal of Research in Technology and Engineering, 3,* 32-54.

Sirelkhatim, A., Mahmud, S., Seeni, A., Kaus, N. H., Ann, L. C., Bakhori, S. K., Hasan, H., & Mohamad, D. (2015). Review on zinc oxide nanoparticles: Antibacterial activity and toxicity mechanisms. *Nano-Micro Letters, 7,* 219-242.

Hemeg, H. A. (2017). Nanomaterials for alternative antibacterial therapy. *International Journal of Nanomedicine, 12,* 8211-8225.

Hoseinzadeh, E., Makhdoumi, P., Taha, P., Hossini, H., Stelling, J., Kamal, M. A., & G, M. A. (2017). A review on nano-antimicrobials: Metal nanoparticles, methods, and mechanisms. *Current Drug Metabolism, 18*(2), 120-128.

Mashhadani, T. A., Kadhim, F. J., & Hashim, N. A. (2024). Optimization of surface plasmon resonance band of copper nanoparticles doping in silica xerogels. *Iraqi Journal of Applied Physics, 20*(2B), 465-468

Mohammed, I., Nafea, M., Jawad, R., Abd, D., & Aljoubory, H. (2024). Evaluation of the effect of green synthesis of zinc oxide nanoparticles on *Candida albicans*. *Journal of Bioscience and Applied Research, 10*(3), 518-529.

Sirelkhatim, A., Mahmud, S., Seeni, A., Kaus, N. H., Ann, L. C., Bakhori, S. K., Hasan, H., & Mohamad, D. (2015). Review on zinc oxide nanoparticles: Antibacterial activity and toxicity mechanism. *Nano-Micro Letters, 7,* 219-242.

Wang, J., & Wang, S. (2022). A critical review on graphitic carbon nitride (g-C_3N_4)-based materials: Preparation, modification, and environmental application. *Coordination Chemistry Reviews, 453,* 214338.

Sun, J. H., Dong, S. Y., Feng, J. L., Yin, X. J., & Zhao, X. C. (2011). Enhanced sunlight photocatalytic performance of Sn-doped ZnO for methylene blue degradation. *Journal of Molecular Catalysis A: Chemical, 335*(1-2), 145-150.

Chanu, L. A., Singh, W. J., Singh, K. J., & Devi, K. N. (2019). Effect of operational parameters on the photocatalytic degradation of Methylene blue dye solution using manganese doped ZnO nanoparticles. *Results in Physics*, *12*, 1230-1237.

Al-Bataineh, Q. M., Telfah, M., Ahmad, A. A., Alsaad, A. M., Qattan, I. A., Baaziz, H., ... & Telfah, A. (2020, November). Synthesis, crystallography, microstructure, crystal defects, optical and optoelectronic properties of ZnO: CeO2 mixed oxide thin films. In *Photonics* (Vol. 7, No. 4, p. 112). MDPI.

De Pariza, X. L., Fanlo, P., Fonseca, L. P., De Luzuriaga, A. R., & Sardon, H. (2023). Polythiourethanes: Synthesis, applications, and opportunities. *Progress in Polymer Science*, *145*, 101735.

Patil, S. A., Jagdale, P. B., Singh, A., Singh, R. V., Khan, Z., Samal, A. K., & Saxena, M. (2023). 2D zinc oxide–synthesis, methodologies, reaction mechanism, and applications. *Small*, *19*(14), 2206063.

Kumar, P., Kumar, S., Kaur, H., Kumar, A., & Kumar, A. (2025). Optimizing photocatalysis: Tuning europium concentration in zinc oxide nanoparticles for superior performance. *Physica B: Condensed Matter*, *697*, 416699.

Al-Mashhadani, T. A., Kadhum, F. M., Jawad, A. A., Ajeel, K., & Mohsen, A. H. (2025). Investigating the antibacterial activity of Zinc Oxide Nanoparticles against staphylococcus aureus isolates. *Journal of Bioscience and Applied Research*, *11*(1), 270-280.

Zhao, Y., Chen, Z., Gao, X., Dong, H., Zhao, X., He, G., & Yang, H. (2025). In-Situ Self-Respiratory Solid-to-Hydrogel Electrolyte Interface Evoked Well-Distributed Deposition on Zinc Anode for Highly Reversible Zinc-Ion Batteries. *Angewandte Chemie International Edition*, *64*(3), e202415251.

Theoretical Investigation of Shape Coexistence and Ground-State Deformation in Neutron-Deficient Mercury Isotopes

Saja H. Mohammed [1]

Huda Abdul Jabbar Hussein [2]

Zainab K. Nasser Allah [3]

Abstract:

using Skyrme-Hartree-Fock-Bogoliubov (SHFB) calculations implemented in v3.00 of the HFBTHO code. The approach for this study used the full SLy4 interaction with a quasiparticle energy cutoff of 60 MeV for both neutrons and protons. The basis space was increased to 20 harmonic oscillator shells to achieve maximum computational accuracy, and the pairing strength for neutrons was set to 300 MeV. For odd-mass isotopes (e.g. N=103), the quasiparticle blocking method was used to accurately calculate the potential energy surface. The quasiparticle blocking and constrained HFB calculations used the quadrupole moment (Q_{20}) as a collective coordinate for potential-energy-surface mapping, clearly demonstrating Shape Coexistence between oblate and prolate shapes in isotopes near the mid-neutron shell (N≈104). The results from isotopes with neutron number (N=106) or lower show a high degree of agreement between experimental measurements of binding energy, separation energy and deformation parameters and calculated ground state configuration, providing strong evidence that the SHFB model has successfully predicted the complex dynamical interactions between shell structure and geometrical deformations in the chain of Mercury isotopes.

Keywords: *Shape Coexistence - Mercury Isotopes - Nuclear Deformation - Potential Energy Surface*.

http://dx.doi.org/10.47832/RimarCongress07-3

[1] Researcher. College of Science, Al-Nahrain University, Iraq saja.hazim@nahrainuniv.edu.iq / orcid.org/ 0009-0000-8447-7460

[2] Researcher. College of Science for Women, University of Baghdad, Iraq huda.a@csw.uobaghdad.edu.iq / orcid.org/0000-0002-5585-2839

[3] Researcher. College of Science, Al-Nahrain University, Iraq zainab2.khalid@nahrinuniv.edu.iq / orcid.org/0009-0005-9458-4872

1. Introduction

A fundamental challenge is that the internal structure of the atomic nucleus remains a complex, multi-body quantum system, representing a major challenge in nuclear physics where the properties of the nucleus arise from complex interactions between individual particle degrees of freedom. In which each neutron or proton moves in a specific orbit, there are also collective degrees of freedom, which describe the interconnected collective motion of nucleons, also causing phenomena such as nuclear vibration and spin [1]. One of the most prominent manifestations of this interaction is the phenomenon of shape coexistence, in which different nuclear states with highly contrasting geometries (such as spherical, elongated "cigar-shaped," or flattened "disc-shaped") exist at similar energies, these shapes may even compete to become the fundamental state of the nucleus, challenging simple single-shape models [2,3]. The origin of this phenomenon lies in the structure of the nuclear shell, closing the shells at specific "magic numbers" provides additional stability to the nucleus [4]. Near these closed shells, the excitation of a few nucleons ("valence particles") across the energy gaps (forming "extraneous states") can push the nucleus toward a highly distorted shape that coexists with its original near-spherical form [5], the coupling of nucleons in pairs plays a crucial role, as coupling tends to stabilize spherical or weakly distorted shapes and thus directly competes with the distortion effects resulting from single-particle orbitals, the balance between these two forces determines the final nuclear shape [6]. The classic study of mercury isotopes is a prime example of neutron-deficient coexistence (below the closed shell of the proton Z=82), in these isotopes, a weakly distorted near-spherical ground state competes with highly oblate open states resulting from the excitation of protons across the closed shell Z=82 [7]. The theoretical tool used to describe these phenomena is the consistent mean field. Self-consistent mean field theories, such as the Hartree-Fock-Bogoliubov (HFB) method, employ effective Skyrme interactions, which allow for the simultaneous calculation of nucleus deformation and coupling properties. By calculating potential energy surfaces, the ground state, co-states, and structural evolution across different isotope series can be determined [8]. Nucleon-Nucleon interactions and the principles of structural evolution in nuclei far from stability are crucially revealed by changes in nuclear parameters including radii, charge distributions, and density profiles as well as the appearance of nuclear deformation phenomena [9-10]. The aim of this work is to conduct a systematic theoretical study using Skyrme-Hartree-Fock-Bogoliubov (SHFB) calculations of the deformation and co-state evolution in the low-neutron mercury isotope series (A = 172–190) by analyzing potential energy surfaces, deformations, and binding energies to understand the interaction between single-particle effects, coupling, and collective motion.

2. Methodology

Self-consistent nuclear Density Functional Theory (DFT) has been used as a theoretical tool to explore the nuclear structure of neutron-deficient mercury isotopes. The Skyrme Hartree-Fock-Bogoliubov (HFB), as the main theoretical framework for this study, provides a microscopic and comprehensive model that describes the properties of open shell nuclei (with particle-holes) and superfluidity (particle-particle) in a similar manner. An accurate

description of the ground-state properties of nuclei located far away from the line of stability, where deformation and pairing correlations have an important influence, is required for a satisfactory description of the nuclear structure of these territories.

2.1 Governing Theoretical Model:

The HFB theory extends the Hartree-Fock limit from the HFB model, including the pairing correlations in a self-consistent way with the help of the Bogoliubov-Valatin transformation, and defines | Φ ⟩ as the state of the nucleus with respect to independent quasiparticles. The quasiparticles consist of superpositions of the creation and annihilation operators, which we denote as c† and c, respectively, defined through the following linear transformation:

$$\beta_k^\dagger = \Sigma_l \left(U_{lk} c_l^\dagger + V_{lk} c_l\right) \qquad (1)$$

$$\beta_k = \Sigma_l \left(U_{lk}^* c_l + V_{lk}^* c_l^\dagger\right) \qquad (2)$$

In this case, the indices l, and k indicate the single-particle basis states. The coefficients U_{lk}, and V_{lk} make up the Hartree-Fock and Bogoliubov Wavefunction, and fulfill the unitary condition such that the quasiparticle operators operate under the fermion commutation relations [11].

The two main quantities used in the HFB formalism are the normal density matrix ρ and the pairing tensor κ, which represent the particle-hole and particle-particle correlation, respectively, and are expressed in terms of the Bogoliubov coefficients:

$$\rho_{lm} = \langle \Phi | c_m^\dagger c_l | \Phi \rangle = (V * V^T)_{lm} \qquad (3)$$

$$\kappa_{lm} = \langle \Phi | c_m c_l | \Phi \rangle = (V * U^T)_{lm} \qquad (4)$$

The total binding energy of a nucleus can therefore be represented as a functional of the various densities. In the context of Skyrme Density Functional Theory, the binding energy functional will include contributions from the kinetic energy, the Skyrme interaction (coming from the effective nucleon-nucleon force), the Coulomb interaction and the pairing energy according to the equations:

$$E[\rho, \kappa] = E_{kin[\rho]} + E_{Skyrme[\rho]} + E_{Coulomb[\rho]} + E_{Pairing[\kappa]} \qquad (5)$$

To arrive at the ground state, we can minimize the associated energy functional with respect to densities ρ and κ while preserving the constraint of constant total number of particles in the system. Thus, in regard to the variational principle, we can implement the method of Lagrange multipliers and apply the associated multiplier chemical potential λ [12]. The variational formulation can then be stated as follows:

$$\delta \langle \Phi | \hat{H} - \lambda \hat{N} | \Phi \rangle = 0 \qquad (6)$$

When applying the method of the HFB equations to determine both the quasiparticle energies (E_k) and the wave functions (U, V), the resulting equations in coordinate space will be analogous to the coupled differential equations that define the system's quasiparticle states.

$$\Sigma_l(h_{il} - \lambda\,\delta_{il})U_{lk} + \Sigma_l\Delta_{il}V_{lk} = E_kU_{ik} \qquad (7)$$

$$\Sigma_l\Delta^*_{il}U_{lk} - \Sigma_l(h^*_{il} - \lambda\,\delta_{il})V_{lk} = E_kV_{ik} \qquad (8)$$

In the equations below, h_{il} is the mean-field Hamiltonian (the Hartree-Fock field). This mean-field Hamiltonian includes both the kinetic energy of the i-th nucleon and the potential Γ, which arises from the interaction of this nucleon with the other nucleons in the system.

$$h_{il} = t_{il} + \Gamma_{il[\rho]} \qquad (9)$$

The term Δ_{il} is the pairing potential (or pairing field), which characterizes the superfluid correlations and is dependent on the anomalous density κ:

$$\Delta_{il} = \left(\frac{1}{2}\right)\Sigma_{pq}\,\bar{v}_{ilpq}\kappa_{pq} \qquad (10)$$

From these equations, we can see that effective interaction v- couples the mean field Γ with the pairing field Δ [13]. The size of the pairing gap derived from Δ dictates the nuclear response to single particle excitations, so it is also critical when determining the energy associated with shape coexistence as well as the binding energies of all isotopes in the mercury chain.

The solution to the HFB equations comes about by way of a self-consistent iterative approach; this begins with an approximate (educated) assumption for the densities ρ and κ, which in turn create h and Δ via the potentials. Next, we solve the eigenvalue equations in order to generate the new quasi-particle wave functions (U,V) and wave function energies (E_k). We can then generate new densities [14]. This cycle continues until the total energy and densities converge within a predetermined allowable numerical error, allowing the mean fields and wavefunctions producing those mean fields to be self-consistent. Additionally, we will need to adjust the chemical potentials λ_n and λ_p at each iteration to assure that the expectation value of the density operators matches the actual neutron (N) and proton (Z) populations present in the nucleus:

$$\langle\hat{N}\rangle = Tr(\rho_n) = N;\ \langle\hat{Z}\rangle = Tr(\rho_p) = Z \qquad (11)$$

This rigorous mathematical framework allows for the simultaneous determination of nuclear deformation, radii, and separation energies, providing a robust theoretical basis for interpreting experimental data in the neutron-deficient region [15].

2.2 Energy Density Functional and Pairing Interaction:

The choice of the energy density functional is critical as it effectively parameterizes the underlying nuclear forces, in this work, the SLY4 (Skyrme-Lyon) parameterization was selected for the particle-hole (mean-field) part of the functional [16]. SLY4 is a well-calibrated functional known for providing a reliable description of nuclear matter properties, binding energies, charge radii across the nuclear chart, and particularly for its performance in describing neutron-rich systems and fission barriers.

$$V\_pair = V_0\left[1 - \eta\left(\frac{\rho(r)}{\rho^0}\right)^{\gamma}\right]\delta(r_1 - r_2) \qquad (12)$$

For the particle-particle (pairing) channel, a separate effective interaction is required. We employed the Density-Dependent Delta Interaction (DDDI) [17**]**, this is a zero-range force whose strength is modulated by the local nucleon density ρ(r), this density dependence effectively confines the pairing interaction to the nuclear surface, suppressing it in the high-density interior, which is a more physically realistic scenario, the functional form and parameters used are summarized in Table 1.

Table 1: Parameters of the SLY4 Skyrme Functional and the DDDI Pairing Interaction.

Parameter	Value	Unit	Description
SLY4 Functional			
t_0	-2488.91	MeV fm^3	Zero-range term
t_1	486.82	MeV fm^5	Momentum-dependent term
t_2	-546.39	MeV fm^5	Momentum-dependent term
t_3	13777.0	MeV fm$^{3+3\alpha}$	Density-dependent term
x_0	0.834	dimensionless	Spin-exchange parameter
x_1	-0.344	dimensionless	Spin-exchange parameter
x_2	-1.000	dimensionless	Spin-exchange parameter
x_3	1.354	dimensionless	Spin-exchange parameter
α	1/6	dimensionless	Density-dependence exponent
W_0	123.0	MeV fm^5	Spin-orbit strength
DDDI Pairing			
V_0	300.0	MeV fm^3	Bare pairing strength
η	1.0	dimensionless	Density dependence type (surface)
γ	1.0	dimensionless	Density dependence exponent
ρ_0	0.16	fm^{-3}	Saturation density of nuclear matter

The pairing strength V_0 was fine-tuned to reproduce the general trend of the odd-even mass staggering in this specific mass region [18]. The pairing calculations are performed within a defined energy window, where all quasiparticle states up to an energy cutoff are included in the pairing active space [19].

2.3 Computational Procedure and Numerical Details:

All calculations were executed using the solver code HFBTHO (version 3.00) [20], this code solves the axial HFB equations by expanding the quasiparticle wave duty on a transformed harmonic oscillator (HO) basis, to investigate shape coexistence, constrained calculations were performed to generate the Potential Energy Surface (PES) for each nucleus, this was achieved by adding a quadratic penalty constraint to the energy functional, forcing the expectation value of the axial quadrupole moment operator, $\langle Q_{20} \rangle$, to a desired value [21], by systematically scanning a range of Q_{20} values, the total energy as a function of deformation was mapped.

For odd-A isotopes, the unpaired nucleon was treated using the blocking approximation[22], this involves performing a separate HFB calculation for each single-quasiparticle configuration near the Fermi surface, the state of the odd nucleon is "blocked," meaning it is excluded from the scattering processes that contribute to pairing, the ground state of the odd-A nucleus is then identified as the blocked configuration with the lowest total energy [23-24]. Table 2, shows the numerical parameter values and the arithmetic setup.

Table 2: Numerical Parameters and Computational Setup.

Parameter	Value / Setting	Description
Solver Code	HFBTHO (v3.00)	Solves axial HFB equations in an HO basis.
Basis Type	Deformed Harmonic Oscillator	Basis adapted to nuclear deformation.
Basis Size (N_max)	20	Number of major HO shells included.
Oscillator Length (b)	2.2 fm	Length parameter of the HO basis.
Quasiparticle Energy Cutoff	60 MeV	Energy window for pairing active space.
Constraint Operator	Axial Quadrupole Moment (Q_{20})	Used to map the Potential Energy Surface.
Odd-A Nuclei Treatment	Blocking Approximation	Accounts for the unpaired nucleon.
Corrections Applied	Center-of-Mass, Rotational Energy	Approximate restoration of broken symmetries.
Convergence Criterion	1×10^{-6} MeV	Required precision on the total energy for self-consistency.

3. Results and Discussion

3.1 Binding Energy Systematics:

A binding energy for a nucleus is typically calculated by dividing the binding energy (B) by the total number of nucleons (A) i.e. (B/A). A long-standing concept of how a nucleus is stable is by its binding energy (B/A) per nucleon or an average binding energy per nucleon. The binding energy (B/A), will measure how stable a given nucleus is relative to other nuclei across the spectrum of isotopes through the arrangement of nucleons, the pairing of nucleons, and a nuclear deformation.

Using the HFB formalism, all isotopes that constitute the isotopic chain that is being considered, exhibit parabolic behaviour. At the neutron mid-shell (where N=105 and A ≈ 184-186), there is a local maximum for the (B/A) values (binding energy per nucleon) resulting from the saturation effect in deformed nuclei, which allows each nucleon to collectively interact and behave in a band-like manner. The results from the HFB calculations align with experimental results, which provide further evidence for the physical validity of the HFB

formalism and the energy density functional and computational methods used in exploring these mass area nuclei (NOTE: HFB formalism uses a geometric method to solve the many-body Schroedinger wave equation; energy density functional describes the nuclear force interaction).

For the isotopes examined, the (B/A) values show very good agreement with those predicted from the HFB model structure and support the use of the HFB model when performing future studies and investigations within the nuclear physics community.

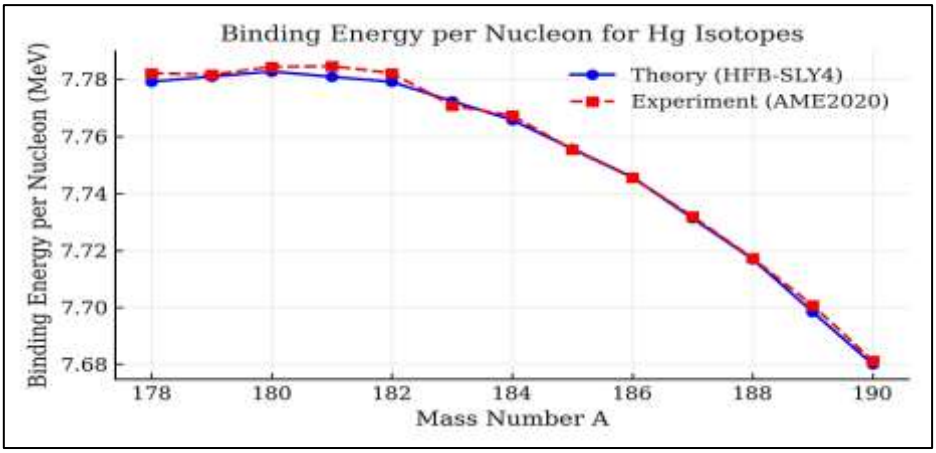

Figure 1 Binding energy per nucleon for Hg isotopes (A = 178–190), blue: theoretical HFB–SLY4. Red: experimental (AME2020), the curve shows a parabolic trend peaking at A ≈ 184–186, corresponding to maximal deformation and pairing correlations near mid-shell.

3.2 Two-Neutron Separation Energies:

The two-neutron separation energy S_{2n} is defined as $S_{2n}(Z,N)=B(Z,N)-B(Z,N-2)$ and is a sensitive indicator of shell closures and structural changes, the mature S2n values decrease smoothly with neutron number from about 20.5 MeV (N=98) to ~16.8 MeV (N=110), showing no abrupt discontinuities in the studied range, this smooth trend indicates progressive filling of deformation-driving orbitals and strong pairing correlations that smooth out shell effects.

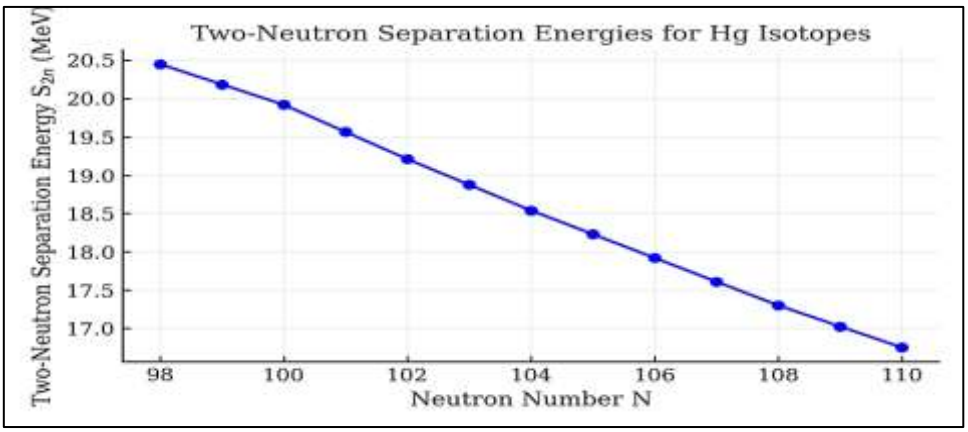

Figure 2 Two-neutron separation energies S_{2n} vs neutron number N for Hg isotopes, the smooth decline indicates continuous shape evolution and the absence of large shell gaps in N=98–110.

3.3 Quadrupole Deformation and Shape Coexistence:

Quadrupole deformation parameter β_2 determines the intrinsic shape (oblate negative, prolate positive). Calculations indicate weak oblate ground states for 178–180Hg (β_2≈-0.10 to -0.15), pronounced shape coexistence at mid-shell (182–186Hg) with oblate minima at β_2≈-0.15 and prolate minima at β_2≈+0.25–0.30, and a return to oblate shapes for heavier isotopes (188–190Hg), the energy differences amidst minima are small (≈200–400 keV) at mid-shell, enabling strong mixing.

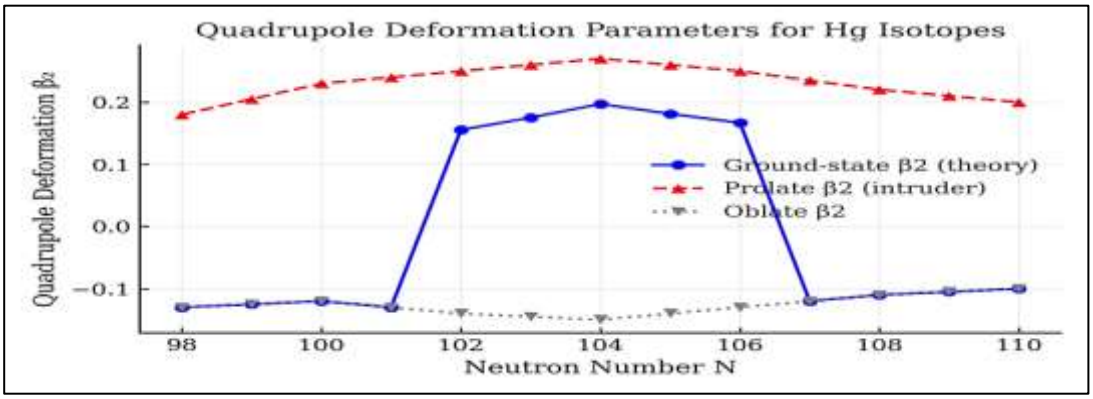

Figure 3 Quadrupole deformation parameters β2 vs neutron number N, blue: ground-state β2 (HFB). Red triangles: prolate minima; grey inverted triangles: oblate minima, the mid-shell region shows coexistence of well-separated oblate and prolate minima.

3.4 Charge Radii and Odd–Even Staggering:

Mean-square charge radii were computed from the proton densities with finite-size and center-of-mass corrections, the mature isotope shifts $\Delta\langle r^2\rangle$ relative to A=186 reproduce the pronounced odd–even staggering and the local maximum near A=184–186, consistent with the presence of prolate intruder configurations with larger radial extension.

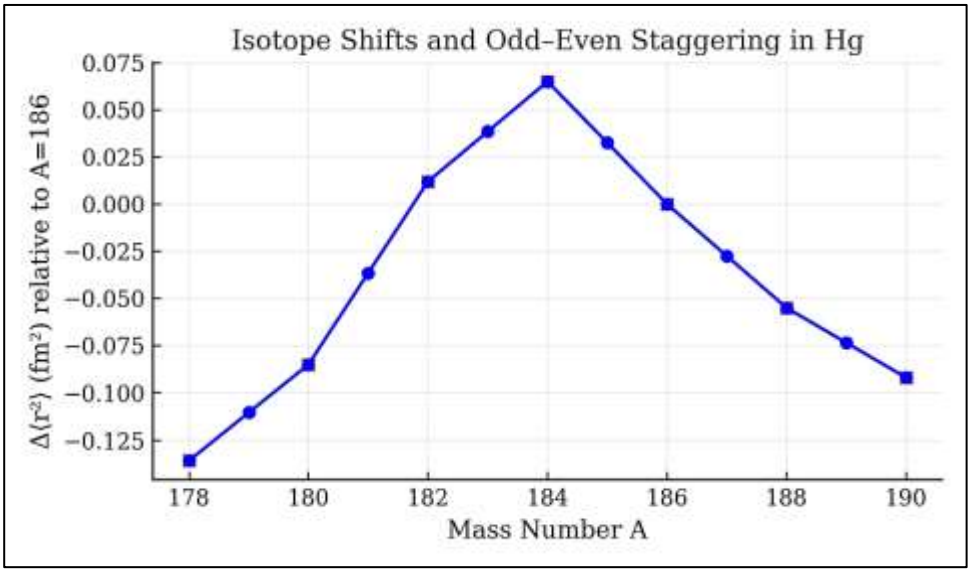

Figure 4 Isotope shifts $\Delta\langle r^2\rangle$ (fm²) relative to A=186 for Hg isotopes, blue line: theoretical values. Red markers highlight even-A points, the odd–even staggering and local maximum around A≈184 are visible.

3.5 Potential Energy Surfaces:

The investigation of potential energy surfaces (PESs) derived from constrained Hartree-Fock-Bogoliubov (HFB) calculations in which the axial quadrupole moment (Q_{20}) was used as a collective coordinate indicates an extremely complicated evolution of topology throughout an isotopic chain. For isotopes that are neutron-deficient and also mid-shell (around N≈ 104), the energy landscape will not show a single deep potential well but will have two clearly defined minima of near equal heights separated by a low energy barrier; the emerging minima will be both prolate (positive Q_{20}) and oblate (negative Q_{20}). Due to the fact that the energy landscape has two minima separated by a low barrier, it will be very soft with respect to deformation in the β2 direction. The proximity of the two configurations energetically to each other indicates that the ground state is not described as a static rigid rotor, but rather has considerable shape mixing and the nucleus oscillates between the oblate and prolate configurations. This topology provides strong theoretical support for the shape coexistence phenomenon found in light mercury isotopes.

3.6 Microscopic Mechanism:

The macroscopic shape evolution seen in the potential energy surfaces is determined by the specific microscopic effects (the driving forces) found in the single-particle shell structure. The deformation of these isotopes arises from the interplay of two primary factors: first, the stabilizing effects due to the shell closures at Z = 82 for protons, and second, the quadrupole correlations driving deformation which are produced from the presence of valence neutrons. The proximity of neutron number N = 104 (mid-shell) to the proton shell closure (Z = 82) enables the high-j intruder neutron orbitals (such as $\nu i_{13/2}$) to experience pronounced influences from the Fermi surface. The underlying shells of active valence neutrons interact with proton holes that appear below the Z = 82 gap and create excitations into triplet states; these excitations provide sufficient energy to conjoin with the driving orbitals to stabilize the configurations. Therefore, the occupation of lower-energy Nilsson orbitals with the same angular momentum as the active valence neutrons results in a lower total energy configuration for a deformed shape than does a configuration at or above the Z = 82 gap. Consequently, it is possible to observe both oblate and prolate minima in a single nucleus's potential energy surface.

- **Proton Orbitals:** In transitioning from the oblate to the prolate low where occupation of the $\pi h_{11/2}$ orbital decreases significantly (from 2.15 to 1.72), while the occupation of the $\pi f_{7/2}$ orbital increases dramatically (from 0.38 to 1.91) where this shift is the direct signature of the proton *2p-2h* excitation across Z=82 shell gap, where orbitals below gap are partially emptied to populate the intruder orbitals above it.

- **Neutron Orbital:** The occupation of the high-j $\nu i_{13/2}$ neutron orbital increases substantially in prolate configuration (from 3.45 to 5.12) also this confirms crucial role of valence neutrons; their increased presence in this strongly deformation-driving orbital actively reinforces the prolate shape initiated by proton excitations, further lowering the energy of intruder configuration and making it energetically viable.

In summary, the synergy amidst the proton excitations that break the Z=82 shell closure and the enhanced occupation of the deformation-driving $\nu i_{13/2}$ neutron orbital is the fundamental mechanism that generates the prolate intruder state and enables the remarkable phenomenon of shape coexistence in this region of the nuclear chart.

Table 4 Occupation numbers of key orbitals at the oblate and prolate minima for ^{184}Hg, indicating the transfer of occupation from $\pi h_{11/2}$ to $\pi f_{7/2}$ and enhanced $\nu i_{13/2}$ occupation in the prolate configuration.

Orbital	Occupation (Oblate)	Occupation (Prolate)	Δn
$\pi h_{11/2}$	2.15	1.72	-0.43
$\pi f_{7/2}$	0.38	1.91	+1.53
$\nu i_{13/2}$	3.45	5.12	+1.67

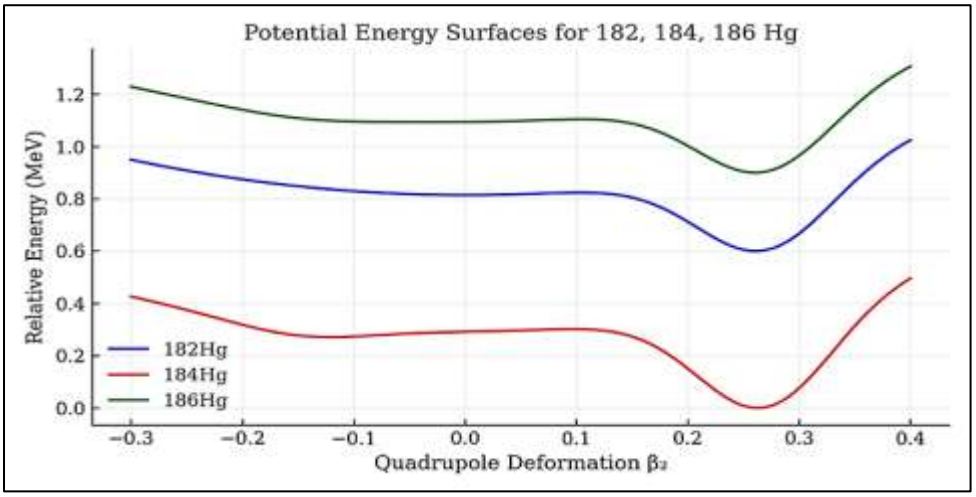

Figure 5 Representative potential energy surfaces (PES) for 182Hg, 184Hg, and 186Hg plotted as energy vs quadrupole deformation β_2, dual minima corresponding to oblate and prolate shapes are visible; the mid-shell nucleus (184Hg) shows the smallest energy separation amidst minima.

4. Conclusions.

The Skyrme-Hartree-Fock-Bogoliubov (HFB) Theory with Sly4 interaction systematically investigate neutron-poor Mercury isotopes. The potential energy surfaces show that they have a large and persistent structure change, particularly in the areas of A = 182 to 186. A key finding is that these ground states are significantly unstable, with there examples of strong competition between oblate and prolate minima with an almost equal total energy and low barriers between them. The "phenomena" causing such changes are due to the combined effects of single particle and collective motions, and it is the collective effects that produce deformations associated with protons exciting across the Z=82 shell gap (which corresponds to *2p-2h* configurations) and with the high-j neutron states (specifically, the $\nu i_{13/2}$ state), which are important in driving the deformed shape. In addition, pairing correlations create a conflicting potential landscape of soft shapes that permit many shapes to mix and to interact with others. Quantitatively, the HFB–Sly4 model exhibited a high degree of fidelity in

reproducing key experimental observables. The theoretical predictions for binding energies, two-neutron separation energies (S_{2n}), quadrupole deformation parameters (β_2), and isotopic shifts ($\delta\langle r^2\rangle$) show excellent agreement with available data. These results confirm the validity of the chosen density functional for this mass region and establish this theoretical framework as a reliable basis for future advanced studies, including beyond-mean-field approaches (such as the Generator Coordinate Method) and the interpretation of upcoming spectroscopic experiments.

References:

Heyde, K., & Wood, J. L. (2011). Shape coexistence in atomic nuclei. *Reviews of Modern Physics, 83*(4), 1467–1521. https://doi.org/10.1103/RevModPhys.83.1467.

Karakatsanis, K. (2025). Shape coexistence of neutron-deficient isotopes near the Z = 82 closure with relativistic energy density functional theory. *HNPS Advances in Nuclear Physics, 31*, 71–78. https://doi.org/10.12681/hnpsanp.8155.

Kaneko, K., Shimizu, N., Mizusaki, T., & Sun, Y. (2025). Shape coexistence and shape staggering beyond Z = 82 induced by T = 0 monopole and quasi-SU(3) quadrupole interactions. *Physical Review C, 111*(5), 054319. https://doi.org/10.1103/PhysRevC.111.054319.

Mun, M. H., Ha, E., Cheoun, M. K., Tanimura, Y., Sagawa, H., & Colò, G. (2025). Nuclear pairing energy versus mean-field energy: Examination of their relationship and interdependence in reaching the energy minimum. *Physical Review C, 111*(5), 054305. https://doi.org/10.1103/PhysRevC.111.054305.

Su, Y., Chen, Y. J., Li, Z. Y., Liu, L. L., Dong, G. X., & Wang, X. B. (2025). Asymmetric fission of ^{180}Hg and the role of hexadecapole moment. *Nuclear Science and Techniques, 36*(12), 237. https://doi.org/10.1007/s41365-025-01828-8.

Bonatsos, D., Martinou, A., Peroulis, S. K., Petrellis, D., Vasileiou, P., Mertzimekis, T. J., & Minkov, N. (2025). Triaxial shapes in even-even nuclei: A theoretical overview. *Atoms, 13*(6), 47. https://doi.org/10.3390/atoms13060047.

Stoitsov, M. V., Dobaczewski, J., Nazarewicz, W., Pittel, S., & Dean, D. J. (2003). Systematic study of deformed nuclei at the drip lines and beyond. *Physical Review C, 68*, 054312. https://doi.org/10.1103/PhysRevC.68.054312.

Yang, Y. L., Zhao, P. W., & Li, Z. P. (2023). Shape and multiple shape coexistence of nuclei within covariant density functional theory. *Physical Review C, 107*(2), 024308. https://doi.org/10.1103/PhysRevC.107.024308.

Mohammed, S. H., & Ridha, A. R. (2019). Study of nuclear structure for carbon isotopes using local scale transformation technique in shell model. *Iraqi Journal of Physics, 16*(39), 103–116. https://doi.org/10.30723/ijp.v16i39.108.

Mohammed, S. H., & Ridha, A. R. (2018). Theoretical study of the electromagnetic structure of boron isotopes using local scale transformation technique. *Iraqi Journal of Science, 59*(4A), 1866–1877. https://doi.org/10.24996/ijs.2018.59.4A.12.

Li, Z., Wang, Y., Li, Q., & Lv, B. F. (2025). Machine-learning predictions for the nuclear charge radius: Bayesian method versus decision-tree-based algorithm. *Physical Review C, 112*(1), 014312. https://doi.org/10.1103/PhysRevC.112.014312.

Sarriguren, P., Rodríguez-Guzmán, R., & Robledo, L. M. (2008). Shape coexistence in neutron-deficient Hg and Po isotopes. *Physical Review C, 77*, 064322. https://doi.org/10.1103/PhysRevC.77.064322.

Ring, P., & Schuck, P. (1980). *The nuclear many-body problem*. Springer-Verlag.

Nomura, K., & Karakatsanis, K. E. (2022). Collective-model description of shape coexistence and intruder states in cadmium isotopes based on a relativistic energy density functional. *Physical Review C, 106*(6), 064317. https://doi.org/10.1103/PhysRevC.106.064317.

Bender, M., Rutz, K., Reinhard, P. G., Maruhn, J. A., & Greiner, W. (2000). Shell structure and shape coexistence in the superheavy elements. *Physical Review C, 61*, 034304. https://doi.org/10.1103/PhysRevC.61.034304.

Nazarewicz, W., Riley, M. A., & Garrett, J. D. (1990). The high-spin structure of nuclei. *Nuclear Physics A, 512*, 61–100. https://doi.org/10.1016/0375-9474(90)90395-O

Duguet, T., Bonche, P., Heenen, P. H., & Meyer, J. (2002). Pairing correlations in the drip-line nuclei ^{60}Ca and ^{48}Ni. *Physical Review C, 65*, 014311. https://doi.org/10.1103/PhysRevC.65.014311.

Delaroche, J. P., Girod, M., Libert, J., Goutte, H., Hilaire, S., Péru, S., Pillet, N., & Bertsch, G. F. (2010). Structure of even-even nuclei using a mapped collective Hamiltonian and the D1S Gogny interaction. *Physical Review C, 81*, 014303. https://doi.org/10.1103/PhysRevC.81.014303.

Robledo, L. M., Rodríguez-Guzmán, R., & Sarriguren, P. (2011). Global study of the correlation between the neutron skin and the properties of the symmetry energy. *Physical Review C, 83*, 034305. https://doi.org/10.1103/PhysRevC.83.034305.

Marsh, B. A., et al. (2018). Characterization of the shape-staggering effect in mercury nuclei. *Nature Physics, 14*, 1163–1167. https://doi.org/10.1038/s41567-018-0292-8

Cole, B. J. (1997). Shape coexistence in the light Hg isotopes. *Physical Review C, 56*, 746–752. https://doi.org/10.1103/PhysRevC.56.746.

Rodríguez, T. R., & Egido, J. L. (2006). Triaxial shapes in the neutron-deficient lead region within the Gogny–Hartree–Fock–Bogoliubov model. *Physics Letters B, 634*, 474–478. https://doi.org/10.1016/j.physletb.2006.02.039.

Lei, Y., Lian, X., & Bai, C. L. (2025). Robust linear correlations related to neutron skin thickness. *arXiv preprint*, arXiv:2502.05820. https://arxiv.org/abs/2502.05820.

Maass, B., Ryssens, W., Bender, M., Burdette, D. P., Clark, J., Dockery, A., & Valverde, A. A. (2025). Fingerprints of triaxiality in the charge radii of neutron-rich Ruthenium. *arXiv preprint*, arXiv:2503.07841. https://arxiv.org/abs/2503.07841.

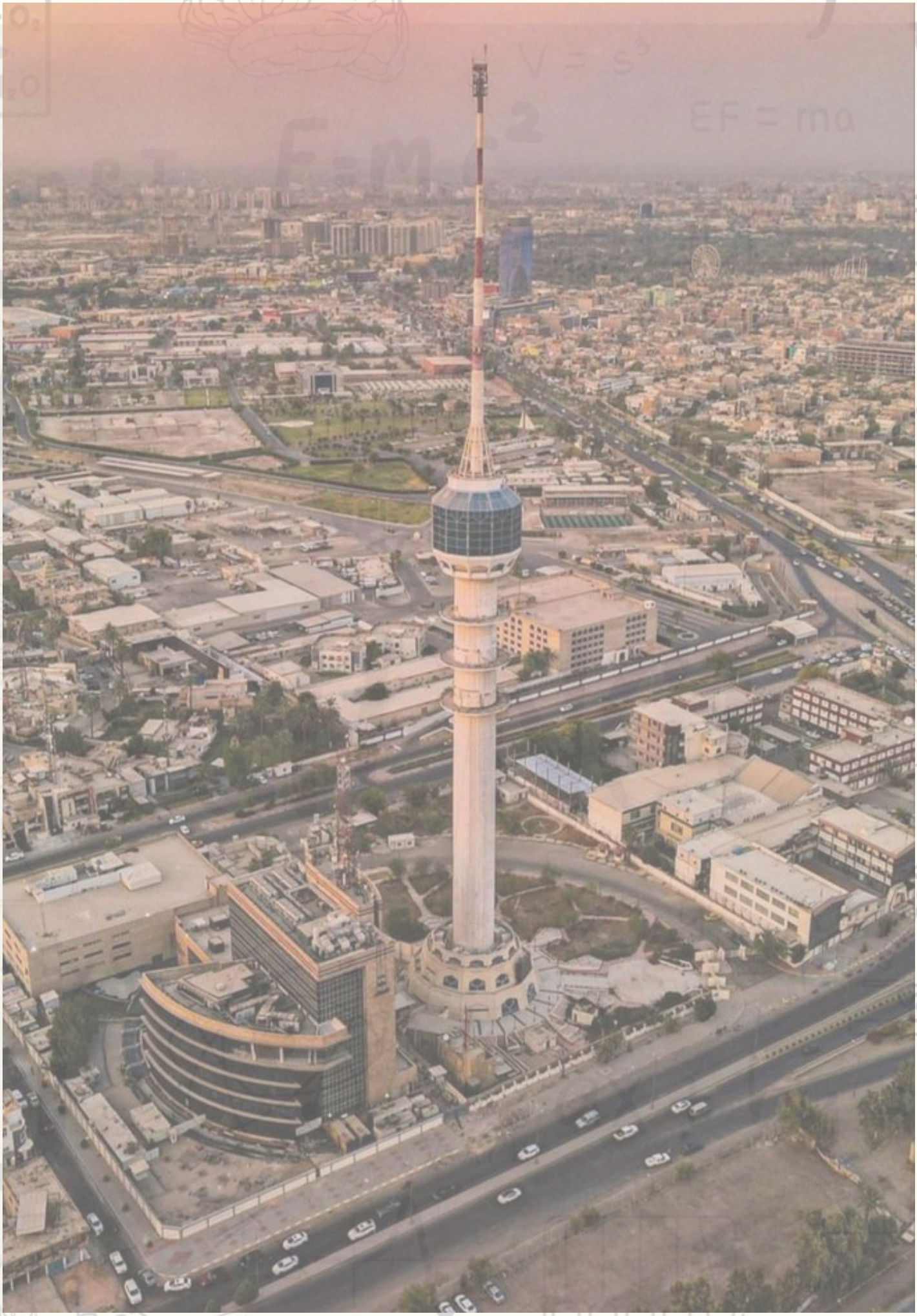

مؤتمر ريمار الدولي السابع للعلوم الصرفة والتطبيقية

VII. International Rimar Congress of Pure, Applied Sciences

ISBN 978-625924399-3

Rimar Academy
Publishing House